

UNIVERSIDAD AUTÓNOMA DE NUEVO LEÓN

FACULTAD DE INGENIERÍA MECÁNICA Y ELÉCTRICA



TESIS

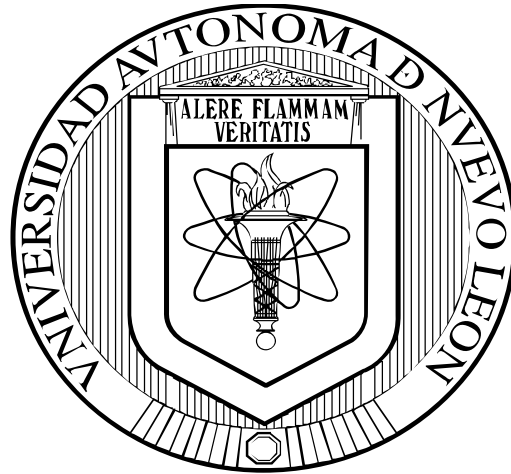
**“EFECTO DE LA MICROESTRUCTURA Y LA CONCENTRACIÓN DEL
ÁCIDO EN LA CORROSIÓN DE ALEACIONES BINARIAS Pb-Sn”**

**PRESENTA
ROCIO BORREGO NAVEJAS**

**EN OPCIÓN PARA OBTENER EL GRADO DE
MAESTRÍA EN CIENCIAS DE LA INGENIERÍA AUTOMOTRIZ**

NOVIEMBRE 2015

UNIVERSIDAD AUTÓNOMA DE NUEVO LEÓN
FACULTAD DE INGENIERÍA MECÁNICA Y ELÉCTRICA



TESIS

**“EFECTO DE LA MICROESTRUCTURA Y LA CONCENTRACIÓN DEL
ÁCIDO EN LA CORROSIÓN DE ALEACIONES BINARIAS Pb-Sn”**

**PRESENTA:
ROCIO BORREGO NAVEJAS**


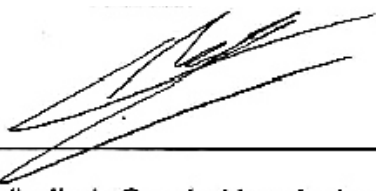
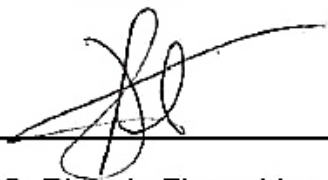
**EN OPCIÓN PARA OBTENER EL GRADO DE
MAESTRÍA EN CIENCIAS DE LA INGENIERÍA AUTOMOTRIZ**

SAN NICOLÁS DE LOS GARZA, NUEVO LEÓN

NOVIEMBRE 2015

UNIVERSIDAD AUTÓNOMA DE NUEVO LEÓN
FACULTAD DE INGENIERÍA MECÁNICA Y ELÉCTRICA
DIVISIÓN DE ESTUDIOS DE POSGRADO

Los miembros del Comité de Tesis recomendamos que la tesis “**Efecto de la microestructura y la concentración del ácido en la corrosión de aleaciones binarias Pn-Sn**” realizada por la alumna Rocio Borrego Navejas con número de matrícula **1651385** sea aceptada para su defensa como opción al grado de Maestra en Ciencias de la Ingeniería Automotriz.

<hr/> Dr. Nelson Garza Montes de Oca Revisor	 <hr/> Dr. Juan Genesca Revisor
 <hr/> Dr. Vladimir García Hernández Revisor	 <hr/> MC. Ricardo Flores Lira Revisor

El comité de tesis
Vo. Bo.

Dr. Simón Martínez Martínez
Subdirector de Estudios de Posgrado

San Nicolás de los Garza, Nuevo León, Noviembre de 2015

AGRADECIMIENTOS

A mis asesores académicos, Dr. Nelson Garza y Dr. Juan Genesca por su confianza, paciencia, apoyo y por dedicarme su tiempo siempre que fue necesario durante todo el proceso de realización de esta tesis.

A mis asesores industriales, Dr. Vladimir García, MC. Ricardo Flores y su esposa Dr. Nora Emma Díaz, por el tiempo dedicado a lo largo de toda la maestría, sus consejos, amistad, paciencia y apoyo incondicional.

A mis compañeros del Laboratorio Global por toda la ayuda que me han brindado durante el desarrollo experimental de esta tesis, Benito González, Sandra Parra, Erandi del Moral, Paul Castillo y sobre todo a Dayra Acosta por todos los conocimientos compartidos, por todas sus recomendaciones y sobre todo, por el tiempo dedicado.

A mis compañeros de maestría Adriana Osuna, Héctor Torres, Fernando López y Marco Delgado por su amistad, consejos, por la experiencia compartida y por los gratos recuerdos de nuestra convivencia durante este tiempo.

DEDICATORIA

A mi esposo Aldo.

TABLE OF CONTENTS

ABSTRACT	8
INTRODUCTION	9
CHAPTER 1 LEAD-ACID BATTERIES	11
1.1 Introduction	11
1.2 Valve Regulated Lead-Acid Batteries	14
1.3 Failure modes of VRLA batteries	17
CHAPTER 2 CORROSION	19
2.1 Introduction	19
2.2 Measurement of corrosion rates	24
2.3 Batteries corrosion	25
CHAPTER 3 Pb-Sn ALLOYS	29
3.1 Introduction	29
3.2 Microstructure of Pb-Sn alloys	31
3.3 Mechanical properties of Pb-Sn alloys	34
3.4 Pb-Sn alloys corrosion	37
CHAPTER 4 EXPERIMENTAL PROCEDURE	43
4.1 Introduction	43
4.2 Experimental plan	43

4.3	Samples	43
4.4	Determination of the chemical composition	45
4.5	Heat treatment of the alloy	46
4.6	Microstructural characterization	48
4.7	Micro-hardness measurements	49
4.8	Determination of mechanical properties	50
4.9	Corrosion rate of the specimens	50
CHAPTER 5 RESULTS AND DISCUSSIONS		53
5.1	Results	53
CHAPTER 6 CONCLUSIONS		65
6.1	Conclusions	65
6.2	Recommendations	66
REFERENCES		67
LIST OF FIGURES		69
LIST OF TABLES		72
APPENDIX		73

ABSTRACT

Lead is a rare element in earth's crust, but since it is found in concentrated deposits it can be produced at low cost, and ranks fifth in tonnage consumed after iron, copper, aluminum and zinc. Some of the many applications of lead are: automobile batteries, uninterruptible power sources, radiation shields in nuclear facilities or medical x-ray apparatus, etc.

For the automobile batteries the common lead alloys are lead-antimony (Pb-Sb), lead-calcium-tin (Pb-Ca-Sn), lead-cadmium-antimony (Pb-Cd-Sb), or lead-tin (Pb-Sn). The Pb-Sn system is the most commonly used for valve regulated lead-acid batteries, which will be the object of study in the current work, which unlike previous works (1; 2) tin content is in a lower % range.

The present work is aimed to study the behavior of Pb-Sn alloys treated under defined conditions of temperature and time as thermal treatments for the study of microstructure and corrosion effects. Once different thermal treatments were applied, its mechanical properties, micro-hardness, microstructure and corrosion rate were evaluated to determine which conditions generate the best performance.

The temperatures used for thermal treatment were 175 and 250 °C with three different cooling temperatures 0, 25 and 50 °C. Once microstructures were evaluated, five samples of each thermal treatment were submitted to measure mechanical properties and another sample was used to determine micro-hardness.

Then, another sample of each thermal treatment was used to evaluate electrochemical properties. Samples of the thermal treatments were tested by electrochemical attack at two different sulphuric acid concentrations to evaluate their corrosion rate.

INTRODUCTION

A battery is a device that converts the chemical energy stored on the active materials directly in electric energy through an oxidation-reduction reaction. This type of reaction involves electrons transfer from one material to other through an electric circuit.

On Valve Regulated Lead-Acid Batteries (VRLA) the connectors and straps are covered by a thin layer of H_2SO_4 solution. Lead is transformed on lead sulphate by the oxidation-reduction reaction over the surface of the element producing the components corrosion (terminal, connectors and grid).

Hypothesis

The effect of the thermal treatment that pieces receive during the manufacturing process modifies its microstructure which is traduced on microstructure modifications leading to mechanical properties and corrosion resistance demission lessening.

Objective

Development and implementation of a methodology that allows to determine the corrosion mechanisms on a Pb-Sn alloy used for recombination batteries.

Specific objectives

- Design a set of experiments to generate different microstructures on a Pb-Sn alloys
- Analysis of microstructure to determine the effect of temperature and time on Pb-Sn binary alloys
- Analysis mechanical properties and micro-hardness to determine the effect of temperature and time on Pb-Sn binary alloys.
- Electrochemical attack at different sulphuric acid concentrations and the measurement of its effect in corrosion through electrochemical methods.

Justification

In the national market the 33% of recombination batteries failures in a lapse of 36 months are produced by corrosion on the connector between plate and terminal.

CHAPTER 1 LEAD-ACID BATTERIES

1.1 Introduction

Electrical energy plays quite an important role in the life of human beings. It can be used in many ways and also can be easily converted into light, heat or mechanical energy. However, an important problem is that this form of energy can hardly be stored. (3)

A battery is a device that converts the chemical energy contained in its active materials directly into electric energy by means of an electrochemical oxidation-reduction (redox) reaction. In the case of a rechargeable system, the battery is recharged by a reversible process. This type of reaction involves the transfer of electrons from one material to another through an electric circuit.

The fundamental elements of the lead–acid battery were set in place over 100 years ago. Gaston Planté was the first to report that a useful discharge current could be drawn from a pair of lead plates that had been immersed in sulfuric acid and subjected to a charging current. Later, Camille Faure proposed the concept of the pasted plate. In subsequent years, the principal elements of the battery have not experienced any further radical changes. The most common design of a battery has ‘flat plates’. These are prepared by coating pastes of lead oxides and sulfuric acid on to conductive lead or lead-alloy ‘grids’, which act as current collectors. The plates are then converted into ‘active’ materials.

The three main components included in a cell are:

1. Anode (negative electrode): fuel or reducing electrode that releases electrons to the external circuit and is oxidized throughout the electrochemical reaction.

2. The cathode (positive electrode): the oxidizing electrode that receives electrons from the external circuit and is reduced throughout the electrochemical reaction.

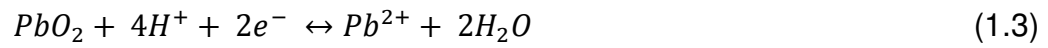
3. The electrolyte: the ionic conductor that supplies the ambient for charge transfer, as ions, inside the cell between the anode and cathode electrode. While the electrolyte is generally a liquid, such as water or other solvents, with dissolved salts, acids, or alkalis to promote ionic conductivity; solid electrolytes, which are ionic conductors at the operating temperature of the cell are also used in some batteries. (4)

The reaction products at the electrodes on charge and discharge of a lead-acid storage battery are as follows:

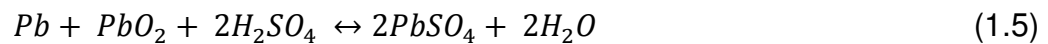
Negative electrode:



Positive electrode:



Overall reaction:



A dissolution-precipitation mechanism is involved in the basic electrode processes occurring in the positive and negative electrodes, and not a solid-state ion transport or film formation mechanism. The discharge-charge mechanism, known as double-sulfate reaction, is also illustrated in Figure 1.1. When H_2SO_4 in the electrolyte is consumed during discharge, water is produced. The electrolyte is an active material and in definite battery designs can be the capacity-limiting material. As the cell approaches full charge and the majority of the $PbSO_4$ has been converted to Pb or PbO_2 , the cell voltage on charge becomes greater than the voltage of gassing (~ 2.39 V per cell) and the overcharge reactions start, resulting in the production of hydrogen and oxygen and the occurrence of water loss. (4)

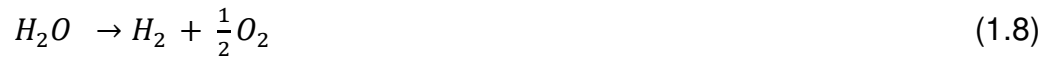
Negative electrode



Positive electrode:



Overall reaction:



Almost any battery, when overcharged, will release hydrogen and oxygen gases in the process of water decomposition. For a battery to be free from maintenance, the prevention of gas evolution is compulsory in order to prevent electrolyte exhaustion which would result in a catastrophic failure. (4)

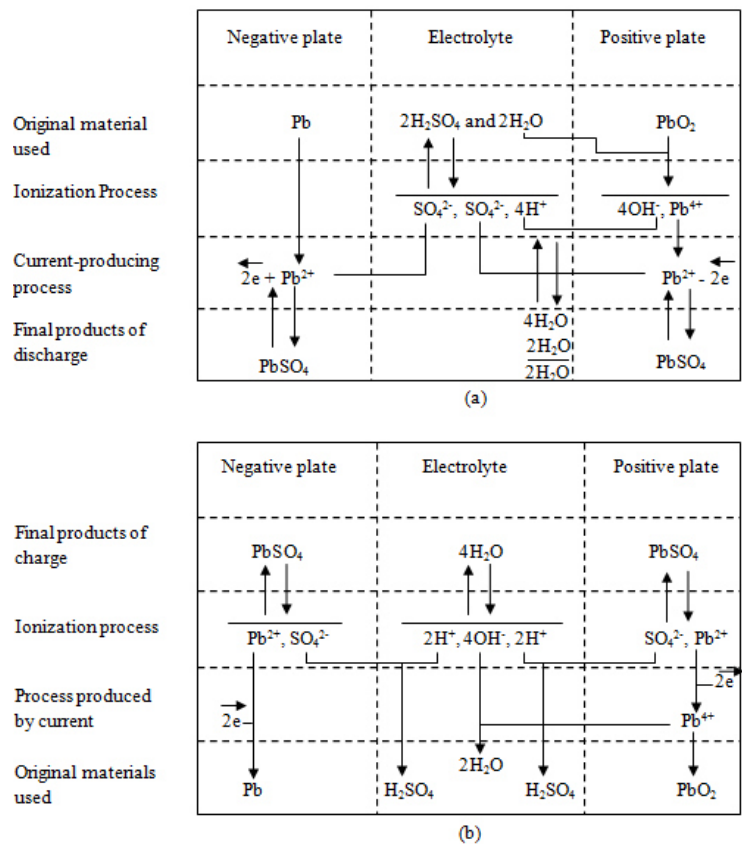
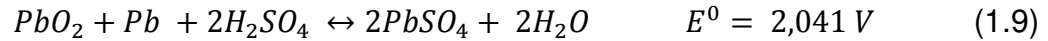
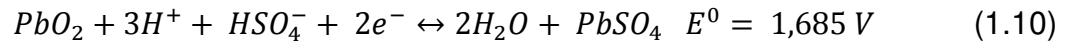


Fig. 1.1 Discharge and charge reactions of lead-acid cell: (a) Discharge reactions; (b) Charge reactions (4)

Overall reaction:



The reaction at the positive electrode:



At the negative electrode:



The charging source driving current through the battery converts finely divided particles of $PbSO_4$ electrochemically to sponge Pb at the negative electrode and PbO_2 at the positive one. When the cell approaches complete recharge, where the majority of the H_2SO_4 has been converted to Pb and PbO , the overcharge reactions begin. For typical lead-acid cells, the result of these reactions is hydrogen and oxygen gases production and subsequent water loss.

1.2 Valve Regulated Lead-Acid Batteries

Lead storage batteries can be classified as conventional type of lead-acid batteries and valve-regulated lead-acid (VRLA) batteries. Conventional lead-acid batteries are “flooded”. This is, the electrolyte is a free liquid which is placed to a level above the top of the plates. This type of batteries have the drawback that the cells have to be vented to release the gases that consist in a very fine mist of highly corrosive sulfuric acid which is liberated during charging, namely, oxygen at the positive and hydrogen at the negative electrode. The disadvantage of this venting is that the batteries should be used only in an upright position; otherwise leakage of sulfuric acid takes place. For many years, efforts have been focused on the development of sealed batteries which would be safer for most of the applications that include them. At first, such attempts includes the catalytic recombination of the gases within the battery; but this approach has not been notably successful. However, invention of VRLA battery brought about the success. In this design, the cell has a starved electrolyte in which the sulfuric acid is immobilized in the separator and the active materials and hence sufficient empty porosity is left for oxygen to diffuse through the separator to the negative plate and recombine back to water. The methods of immobilizing the electrolyte between the plates in VRLA cells are to use gel and absorptive glass micro-fiber

(AGM) type electrolytes. The VRLA battery can be set in any orientation, and thus a much greater degree of flexibility is likely to be attained by design engineers. (5)

The development and marketing of VRLA batteries over the last 40 years has rapidly become widespread given that with their properties most of the needs of many new applications are covered owed to their maintenance-free characteristics, enhanced safety, high-rate capability and high volume efficiency compared with the conventional, flooded-electrolyte batteries. (5)

The VRLA battery is designed to operate by means of an 'internal oxygen cycle' (or 'oxygen-recombination cycle'), see Figure 1.2. Oxygen evolved during the latter stages of charging, and during overcharging, of the positive electrode, i.e.,

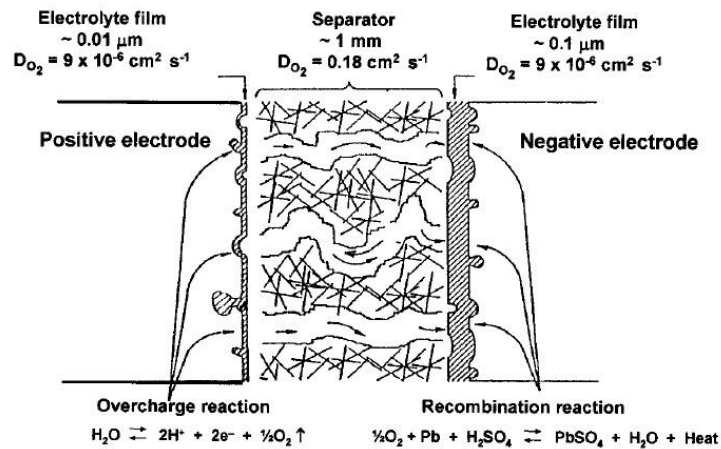
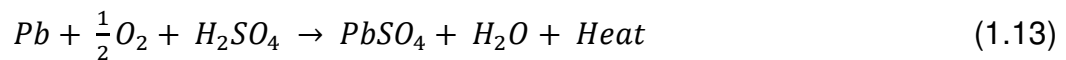


Fig. 1.2 Conceptual view of internal oxygen cycle in a valve-regulated lead–acid cell (6)

Transfers through a gas space to the negative electrode where it is reduced ('recombined') to water:



Two other reactions must be taken into account during the charging of a VRLA cell. These are, the evolution of hydrogen at the negative plate:



And the corrosion of the positive grid:



Thus, the charging of a VRLA cell is potentially more complex than the charging of its flooded counterpart. During the charging of a VRLA cell, thermodynamic/kinetic conditions allow the progress of six separate reactions at significant rates: two charge reactions (the reverse of reactions (1.10) and (1.11)) and four secondary reactions (1.12) to (1.15).

The oxygen cycle, shown in equation (1.12) and (1.13), shifts the potential of the negative electrode to a less negative value and thus decreases the rate of hydrogen evolution to a much lower level (i.e., much less than in the older, flooded design of battery). A one-way, pressure-relief valve is provided to ensure that even the small amounts of hydrogen produced do not generate a high pressure within the battery-hence, the term: 'valve-regulated'. Since the plate is simultaneously on charge, the lead sulfate produced is immediately reduced to lead via the reverse of reaction (1.11). This restores the chemical balance of the cell, i.e., in stoichiometric terms, the net sum of reactions (1.12), (1.13) and the reverse of reaction (1.11) is zero. Thus, part of the electrical energy delivered to the cell is consumed by the oxygen-recombination cycle and is converted into heat rather than into chemical energy. As long as the overcharge current remains moderate, the charge and recombination reactions can remain in equilibrium and little net gas is generated.

There are two alternative designs which provide the gas space in VRLA cells. One design has the electrolyte immobilized as a gel; the other has the electrolyte held in an AGM separator. Gas passes through fissures in the gel, or through channels in the AGM (Figure 1.2).

Antimony is no longer included in the grid alloys for VRLA cells because this element lowers the hydrogen overpotential and therefore encourages gassing at the negative electrode. Care needs to be taken against the introduction of other elements that might act similarly. Excessive gassing at either the negative or the positive electrode can result in selective discharge of the respective electrode. Lead-calcium-tin alloys are preferred by manufacturers of VRLA batteries for float duties, and lead-tin alloys for cycling applications.

If the cell is over-filled with acid initially, the oxygen cycle cannot function because oxygen diffuses through the aqueous phase at a rate which is approximately four orders of magnitude slower than through the gas space, see

Figure 1.2. The cell then behaves as if it were of a conventional, flooded design. Towards top-of-charge, first oxygen (from the positive), and then oxygen (from the positive) and hydrogen (from the negative), are evolved and may be released through the valve. This loss of water eventually opens gas spaces (due to drying out of the gel or a decrease in the volume of electrolyte held by the AGM) and allows the transfer of oxygen to proceed. Gas release from the cell then falls to a very low level.

If the oxygen cycle is worked too hard then substantial heat is generated, charging of the negative plate becomes difficult, and progressive sulfidation begins from the bottom of the plate where the acid concentration tends to be highest. The function of the oxygen cycle is subtly linked to the microstructure of the separator material (for AGM designs) and to the nature of the charge algorithm applied, especially near top-of-charge. (6)

1.3 Failure modes of VRLA batteries

The results from the technology changes from the flooded to the valve-regulated design suggest that most of the failure mechanisms that were discussed earlier in this work may reappear. Hence they are mentioned in the following line in order of importance.

Failure mode 1. Replacement of lead-antimony alloys with lead-calcium alternatives, as a way to discourage hydrogen evolution, reduces the creep strength of grids so that expansion in the plane of the plate may again become a concern. The use of a separator with insufficient rigidity (i.e., too much 'compressibility') may allow expansion normal to the plane of the plate.

Failure mode 2. Water loss can be reduced to the extent that periodic replenishment, as it is required by flooded cells, will be no longer necessary. Nevertheless, both hydrogen evolution at the negative electrode and grid corrosion at the positive electrode could cause some water loss.

Failure mode 3. Any acid stratification that could occur cannot be solved by overcharging because electrolyte availability is resulting in an ineffective mixing. Moreover, water losses cannot be solved because the battery is expected to remain sealed for the entire active life.

Failure mode 4. The operation of the oxygen cycle may cause incomplete charging of either the negative or the positive plate. (7)

In 2002, R. J. Ball performed an investigation into the failure of a series of cycled 40 Ampere-hour (Ah) valve regulated lead-acid batteries and identified the following different types of defects:

- Cracking adjacent to grid bar corners
- Internal boundary cracks within the corrosion layer
- Small fissure cracks
- Small penetrating cracks and oxide fingers

The variation in different types of defects suggests there is more than one mechanism for defect initiation and further expansion. Defects will often occur due to stresses within the corrosion layer. Therefore it is expected that they can expand to a major damage due to the following reasons:

1. Thermal cycling of the oxide due to changing heat generation rates at different periods of the discharge/charge cycle
2. Geometrical (volume) changes associated with the conversion of lead oxide to sulphate during cycling
3. Oxygen gas evolved during overcharging pressurizing and escaping through the oxide corrosion layer. (8)

CHAPTER 2 CORROSION

2.1 Introduction

The word corrode is derived from the Latin *corrodere*, which means “to gnaw to pieces”. The general definition of corrode is to eat into or wear away gradually, as if by gnawing. For purposes here, the corrosion phenomenon can be defined as a chemical or electrochemical reaction between a material, usually a metal, and the environment surrounding it leading to a considerable deterioration and important detrimental changes in its properties. (9)

For corrosion to take place, the presence of both anodic and cathodic processes is necessary. Corrosion processes are controlled by both thermodynamics and kinetics which are related to the fundamental feasibility of the reaction and the rate at which occurs. The chance for a thermodynamic reaction to occur can be calculated from the free energy change reaction (ΔG) and, the electrochemical (or cell) potential of a reaction, E or E_{corr} , at equilibrium which can be described by the equation:

$$\Delta G = -zFE_{corr} \quad (2.1)$$

Where z the number of electrons is present in the reaction, and F is the Faraday's constant. The electrochemical potential of a reaction E_{corr} , is the algebraic sum of the half-cell reaction potentials of anodic and cathodic reactions, defined as E_a and E_c , respectively. Since E_{corr} is defined to be positive for a spontaneous reaction, equation (2.1) correctly expresses a decrease in Gibbs function, which is the thermodynamic criterion for a spontaneous reaction at constant temperature, T and pressure, P . When determining the spontaneous direction of an electrochemical reaction, the E_a and E_c , values are calculated according to the standard half-cell electrode potentials at unit activity because of the

concentration changes by the Nernst Equation for a general half-cell reaction, given as: (10)



$$E = E^0 - \frac{RT}{zF} \ln \frac{(B)^b(H_2O)^d}{(A)^a(H^+)^m} \quad (2.3)$$

Where R is the universal gas constant $8.314\ 472(15)\ \text{J K}^{-1}\ \text{mol}^{-1}$, T is the absolute temperature, z is the number of moles of electrons transferred in the cell reaction or half-reaction and F is the Faraday constant, the number of Coulombs (C) per mole of electrons $96485.33289(59)\ \text{C mol}^{-1}$.

2.1.1 The Faraday and Faraday's Law

The process of corrosion involves simultaneous charge transfer and mass transfer across the metal/solution interface. (11)

The unit of charge is the Coulomb (C), which is the product of the current I and its time of passage t . The unit of mass is, of course, the gram, which can be obtained from the number of equivalents of metal lost and the equivalent weight of the metal.

The link between charge transfer and mass transfer is the Faraday F relationship:

$$F = \frac{96,485.33\ \text{C}}{\text{equivalent}} \quad (2.2)$$

Faraday's law states that the mass W of metal corroded is given by

$$W = \frac{I t A}{n F} \quad (2.3)$$

Where I is the electrical current in amperes, t is the time in seconds, A is the atomic weight of the metal, and n is the number of equivalents transferred per mole of metal. (11)

2.1.2 Electrochemical Kinetics of Corrosion

The rate at which an electrochemical reaction occurs or its kinetics is fundamental in the determination of the corrosion rate of a metal subjected to a corrosive medium that is electrolyte; on the contrary, although corrosion feasibility is predicted by thermodynamics, it does not give any information on the ways of occurrence of slower or faster corrosion rate. Since the reaction kinetics on the surface of an electrode depends on the electrode potential, the rate of electron flow to or from a metal-electrolyte interface determines the reaction rate. If the electrochemical system is at equilibrium then the net rate of reaction is equal to zero. Chemical kinetics controls reaction rates whereas electrochemical kinetics mainly controls corrosion rates. (12)

2.1.3 Energy Distribution

The only difference between the forward (ΔG_f) and reverse (ΔG_r) reactions is the change in activation energy for each reaction. Energies for them are shown in Figure 2.1 represent Boltzmann or Maxwell-Boltzmann energy distribution of reversible electrodes of the reacting species (ions). If an overpotential polarized them by under steady-state conditions, the reactions rate is not equal, $R_f \neq R_r$. (12)

Commonly, reaction rates of the electrochemical and chemical resulted from either overpotentials of anodic or cathodic can be anticipated by using both Faraday R_F and Arrhenius R_A equations, respectively as depicted below:

$$R_F = \frac{i A_j}{z F} \quad (2.4)$$

$$R_A = \gamma_a \exp\left(-\frac{\Delta G^*}{RT}\right) \quad (2.5)$$

Where i is the applied current density ($\frac{A}{cm^2}$), whereas A_j is the atomic weight of species j (g/mol), $A_{alloy} = \sum f_i \frac{A_j}{z_i}$ in units of g/mol, j_z and j_f are the valence number and weight fraction of element j , γ_a is the constant of chemical, ΔG^* is the activation energy of free energy change (j/mol).

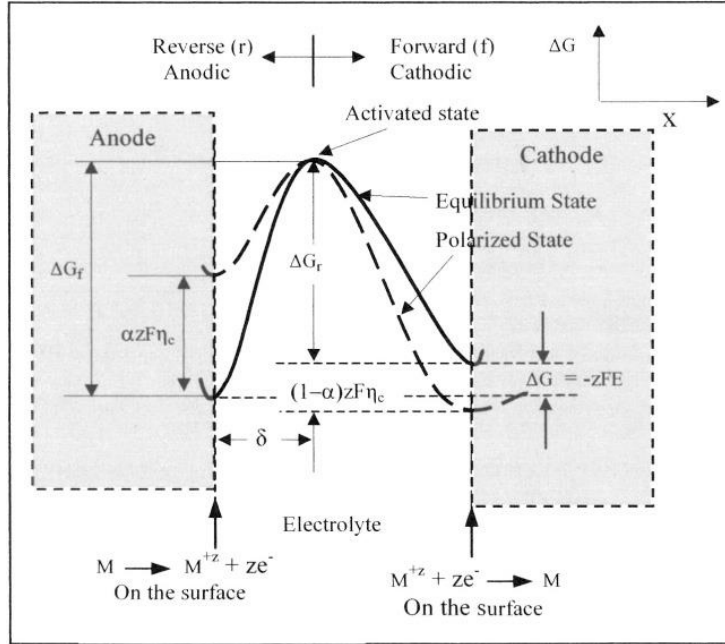


Fig. 2.1 Schematic representation of anodic and cathodic polarization (12)

At equilibrium, rate equations of Faraday and Arrhenius become equal and as a result, the current density becomes:

$$i = \gamma_0 \exp\left(-\frac{\Delta G^*}{RT}\right) \quad (2.6)$$

For a reversible electrode at equilibrium, the current density in equation (2.6) turns out the exchange current density; that is $i = i_0$. (12)

On the other hand, when an overpotential polarized an electrode under steady-state conditions, the reactions rates are not equal $Rf \neq Rr$ and therefore, the forward (cathodic) and reverse (anodic) current density must be described in terms of free energy change, ΔG^* , obtained from Figure 2.1. Therefore,

$$i_f = k'_f \exp\left[-\frac{\Delta G_f^*}{RT}\right] \quad \text{Cathodic} \quad (2.7)$$

$$i_r = k'_r \exp\left[-\frac{\Delta G_r^*}{RT}\right] \quad \text{Anodic} \quad (2.8)$$

Where $\Delta G_f^* = \Delta G_f - \alpha zF\eta_c$, $\Delta G_r^* = \Delta G_r + (1 - \alpha)zF\eta_a$, α is a symmetry coefficient. Where, η_c is the cathodic overpotential, η_a is the anodic overpotential and F is the Faraday's constant. (12)

For the cathodic reaction, the net current and the overpotential are $i = i_f - i_r$ and η_c , respectively. Substituting the equations (2.7) and (2.8) into this expression gives the net current density in a common form given by,

$$i = k'_f \exp\left(-\frac{\Delta G_f}{RT}\right) \exp\left(\frac{\alpha z F \eta_c}{RT}\right) - k'_r \exp\left(-\frac{\Delta G_r}{RT}\right) \exp\left[-\frac{(1-\alpha) z F \eta_a}{RT}\right] \quad (2.9)$$

The exchange current density is defined as

$$i_0 = k'_f \exp\left(-\frac{\Delta G_f}{RT}\right) = k'_r \exp\left(-\frac{\Delta G_r}{RT}\right) \quad (2.10)$$

By substituting equation (2.10) into (2.9) for one-step reaction we obtain the well-known Butler-Volmer equation (2.11) to polarize an electrode from the open circuit potential E_0 under steady-state conditions, where $\eta = E - E_0$. (12)

$$i = i_0 \left\{ \exp\left[\frac{\alpha z F \eta_a}{RT}\right]_f - \exp\left[-\frac{(1-\alpha) z F \eta_c}{RT}\right]_r \right\} \quad (2.11)$$

2.1.4 Electrochemical Polarization

Electrochemical polarization (usually referred to simply as “polarization”) is the change in electrode potential due to the flow of a current. There are three types of polarization:

1. Activation polarization which is polarization caused by a slow electrode reaction.
2. Concentration polarization which is polarization caused by concentration changes in reactants or products near an electrode surface.
3. Ohmic polarization which is polarization caused by IR drops in solution or across surface films, such as oxides (or salts).

The degree of polarization is defined as the overvoltage (or overpotential) η given by the following equation:

$$\eta = E - E_0 \quad (2.9)$$

Where E is the electrode potential for some condition of current flow and E_0 is the electrode potential for zero current flow (also called the open-circuit potential, corrosion potential, or rest potential). Note that the electrode potential of zero current flow E_0 should not be confused with the standard electrode potential E^0 , which plays a prominent role in corrosion thermodynamics. (11)

2.1.5 Anodic and Cathodic Polarization

Either an anode or a cathode can be polarized:

Anodic polarization is the displacement of the electrode potential in the positive direction so that the electrode acts more anodic.

Cathodic polarization is the displacement of the electrode potential in the negative direction so that the electrode acts more cathodic.

These processes are represented schematically in Figure 2.2. (11)

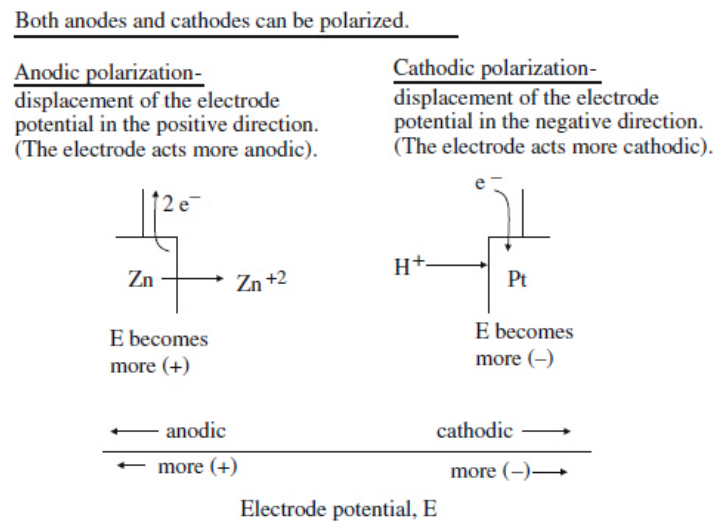


Fig. 2.2 Schematic representation of anodic and cathodic polarization (11)

2.2 Measurement of corrosion rates

Potential-pH Diagrams (Pourbaix diagrams) are a useful first guide as to the corrosion behavior of many different systems. However, Pourbaix diagrams do not give information on the corrosion rates, although a given reaction may be spontaneous, it does not necessarily proceed at a fast rate. The reaction may in fact proceed “slowly” rather than “quickly”, but it is not possible to determine this difference from thermodynamics alone. (11)

Electrochemical techniques have this capability and also offer the possibility of mitigating the corrosion rate, but this chapter will consider only the direct current (DC) polarization method and its variations. (11)

2.3 Batteries corrosion

Corrosion of lead in principle starts at the equilibrium potential of the negative electrode. At a more positive potential lead (Pb) is no longer stable as a metal but is converted into the divalent Pb^{2+} that forms lead sulfate (PbSO_4) according to



Which equals the discharge reaction of the negative electrode, and its equilibrium potential is $U^{\circ}_{\text{Pb}/\text{PbSO}_4} = -0.3 \text{ V}$. (3)

During charging or float charging, the potential of the negative electrode is below this value and corrosion according to Eq. (2.10) is not possible. This applies not only to the grid, but also to the conducting elements as long as they are connected with the electrolyte ('cathodic corrosion protection'). This usually is true in flooded batteries, where the conducting elements are submerged into the electrolyte or covered by a wetting layer of acid that continuously is replenished by acid fumes and remain electrically connected to the electrolyte by ionic conductivity. In valve-regulated lead-acid batteries, however, due to the immobilized electrolyte, the plate lugs and the other conducting elements cannot be submerged into the electrolyte and the wetting film is diluted by the formation of water. Then the potential of the wetting layer may be shifted to more positive values and the cathodic corrosion protection may be lost and corrosion occurs as indicated in Figure 2.3. (3)

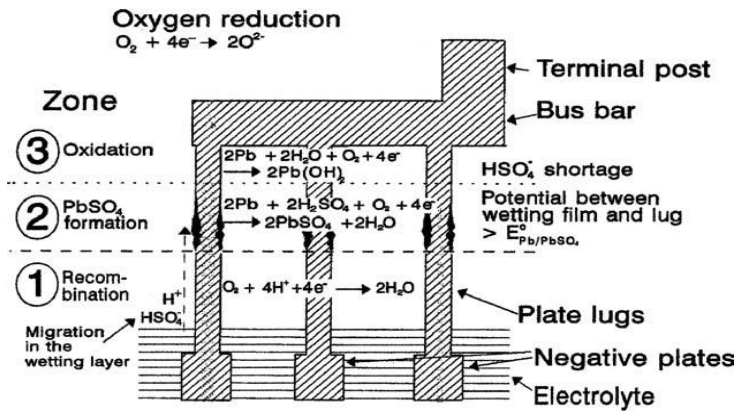


Fig. 2.3 Corrosion at negative plate lugs that occasionally is observed. Current flow along the wetting layer of the non-immersed parts causes a potential shift within that layer. Thus, 'cathodic corrosion protection' may no longer exist above a certain distance from the electrolyte level. The situation is influenced by the alloys used in the parts and for welding (3)

The continuous oxygen reduction at the wetted lead parts has the following results:

- Oxygen reduction on the lugs and the connecting bus bar consumes H^+ ions and causes a current along the wetting film, and thus a voltage drop along the wetting film that displaces the potential in the upper part of the film to more negative values.
- The potential of the metallic parts is uniform. On account of the potential shift along the wetting film, the potential between that film and the metallic surface is increased with the distance from the electrolyte surface (an increase of as much as 200 mV has been observed). Referred to its wetting film, the potential of metal gets more and more positive, and at a given distance it reaches and even exceeds the $Pb/PbSO_4$ equilibrium value (Zone 2 in Figure 2.3). (3)

As a result, three different zones can be observed:

Zone 1: The potential of the metal versus its electrolyte film is below the $Pb/PbSO_4$ equilibrium potential, under this conditions, lead is stable and reduction of oxygen is neutralized by recombination with H^+ ions to H_2O .

Zone 2: When the potential difference between the metal and its wetting layer reaches the $Pb/PbSO_4$ equilibrium potential or is more positive, Pb^{2+} ions are formed, and oxygen reduction is balanced by $PbSO_4$ formation. The situation is

aggravated as the acid in the wetting layer at lug and group bar becomes diluted by the generated water. This dilution decreases the conductivity of the wetting layer and increases the voltage drop along the layer. Furthermore, corrosion roughens the surface and that again increases current and voltage drop. Thus the progressing corrosion accelerates the process.

Zone 3: in Figure 2.3 is characterized by a lack of HSO_4^- ions that are required for the formation of lead sulfate. Lead can only be oxidized. Because of the higher vapor pressure of this nearly neutral region compared to the acid electrolyte, drying converts the $\text{Pb}(\text{OH})_2$ into PbO and finally stops further oxidation.

Depending on the alloys used, severe corrosion occurs in Zone 2. To overcome this issue, bus bars can be wrapped by a glass felt to preserve the contact with the electrolyte and so preserve the 'cathodic corrosion protection'. The selection of welding alloys is also important. (3)

In valve-regulated lead-acid batteries of the absorptive glass mat (AGM) type, the connecting strap (top lead) and the plate lugs are covered by a thin liquid film of H_2SO_4 solution. The H_2SO_4 is consumed during the formation of a lead sulfate corrosion layer. The liquid film has high ohmic resistance, hence the strap and the plate lugs are cathodically unprotected. As a result of this, the life of the battery is limited by corrosion of the negative semi-block (plate group) top lead. Lead-tin alloys are used for the production of the straps for the above battery type. It has been established that the potential of that part of the electrode immersed in the H_2SO_4 solution controls the potential of the electrode up to a height of 1 cm above the solution level. The corrosion layer formed on the electrode surface above the solution (in the air space) gives origin to zones of different phase compositions. It is a common practice to add Na_2SO_4 to the electrolyte of batteries operating at remote locations (e.g., in the mountains) to improve the conductivity of the solution on deep discharge cycling. (13)

During battery operation, the positive grids are attacked by corrosion (25-35%) and the additives and impurities contained in the grid alloy get into the corrosion layer, and become part of the composition of the formed active masses thus affecting the electrochemical processes. The negative grids are not subjected to corrosion, but the alloy components and impurities on the grid surface are in contact with the electrolyte and may become active centers for the electrochemical reaction of hydrogen evolution increasing water loss in the battery by this means. To avoid this problem, the negative grid alloy should contain no impurities which facilitate gassing. Corrosion of the straps and connectors is a slower process. Hence, the additives and impurities in the lead alloys used for the manufacture of straps and connectors have the weakest effect. (13)

2.3.1 Intergranular corrosion

The corrosion characteristics of alloys are determined by both the crystal structure and the chemical composition. Since grain boundaries are chemically more active, corrosion occurs preferentially at the grain boundaries resulting in a phenomenon named intergranular corrosion. The grain boundary area is greater for small grains and, hence, corrosion occurs uniformly throughout the surface. For large grains, there are only a few grain boundary regions and thus corrosion can penetrate deep into the material and give rise to catastrophic failure. (14)

Intergranular corrosion is a specialized type of attack that takes place at the grain boundaries of a metal. Little or no attack is observed on the main body of the grain. The grain boundary material, which is a limited area, acts as an anode, and the larger area of grains acts as cathodes. This results in the flow of energy from the small anode area to the large cathode area, which causes rapid attack penetrating deeply into the metal. (15)

The grain boundary region is an area of crystallographic mismatch between the orderly structures within the adjacent grains. Because of this, it is slightly more active than the grain area. Under certain conditions, the grain boundaries remain very reactive; and under corrosive conditions, the attack along the grain boundaries results in intergranular corrosion (IGC). (15)

The following factors contribute to the increased the reactivity of the grain boundary areas:

1. Segregation of specific elements or compounds, as in aluminum alloys or nickel-chromium alloys
2. Enrichment of one of the alloying elements at the grain boundary, as in brass
3. Depletion of the corrosion-resistant element at the grain boundary, as in stainless steels

All the factors that lead to intergranular corrosion are the result of the thermal exposure of the metals, such as in welding, stress relief, and other heat treatments. (15)

CHAPTER 3 Pb-Sn ALLOYS

3.1 Introduction

Lead alloys are used for casting grids, straps, terminal posts and connectors for lead-acid batteries. The plate grids have two major functions:

- They are the 'backbone' that mechanically supports the active material of the two electrodes.
- They play the role of 'blood system' through which the current flows from and to every part of the plate. (13)

Early grid materials for valve-regulated lead-acid (VRLA) batteries consisted of pure lead or lead-calcium alloys for both the positive and negative plates. Although batteries manufactured with plates that used these grid materials were found acceptable for float applications, a rapid reduction in their performance was observed in cycling duties, often within the first 50 cycles. This phenomenon was named the 'antimony-free effect', but later was known as 'premature capacity loss' (PCL). Two theories were proposed to explain this phenomena. This first was related to the formation of electrically resistive layer of $\text{PbSO}_4/\alpha\text{-PbO}$ at the grid-active material interface in the absence of sufficient antimony in the positive grid. The premise suggested that capacity loss was due to excessive corrosion, and growth, of the positive grid that resulted in inadequate attachment of the active material (lead dioxide). (7)

It was found that the addition of tin to pure lead and lead-calcium alloys improved their mechanical properties, increased the rechargeability, reduced corrosion, and increased the conductivity at the grid-active material interface. When added in proper amounts, tin also modified the grain structure of the grid

materials, changed the method of precipitation of the alloys, and decreased the amount of PbSO_4 or $\alpha\text{-PbO}$ formed at the interface in considerable amount. (7)

Lead-tin alloys are widely used in the cast-on-strap technology for the manufacture of connector straps or for the production of terminals for maintenance-free VRLA batteries. The Sn content of alloys for these applications varies between 0.8 and 2.5 wt% Sn. If Pb-Sn alloys with low Sn concentration are used for the cast-on-strap process, it may yield to unreliable strap-to-lugs connections. To avoid this problem, the grid lugs are previously plated with a lead-tin solder alloy (pretinning). Then they are placed on the mold for casting the strap and connecting it to the plate lugs. (13)

The Pb-Sn binary phase diagram (Figure 3.1) has an eutectic at a temperature of 183°C and a composition of 61.9 wt. % Sn. The solid solubility of Sn in Pb at 183°C is about 19 wt. %, which decreases to 1.3 ± 0.5 wt. % at room temperature. Similar to Pb-Sb alloys, significant age hardening can be obtained in these alloys. On cooling from the single-phase region to room temperature, streaky and granular Sn precipitates are obtained in a matrix of Pb in alloys containing from 1.3 to 19.2 wt. % Sn. Coring can lead to the presence of the eutectic phase in low-Sn-content alloys. Pb-Sn alloys do not take the gray appearance of pure lead, even when stored. (16)

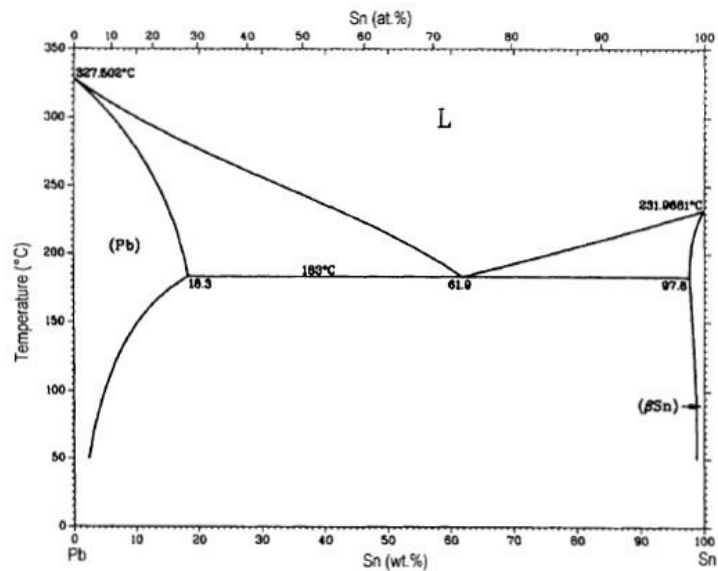


Fig. 3.1 Pb-Sn Phase diagram (16)

Tin alloys of lead have much lower densities and melting points than pure lead. Both density and liquidus temperature decrease as more tin is added, until the eutectic composition (approximately 63% Sn, 37% Pb) is reached. Their lower melting point and increased strength have made the high tin alloys especially important as solders. Nevertheless, the alloys used mainly for corrosion resistance are reduced in tin, the most important alloy, terne, having a composition of 12-20% Sn. Terne is used to coat steel to make what is called a terneplate or terne metal. Tin “wets” the steel, allowing the formation of a metallurgical bond between lead and steel. (16)

3.2 Microstructure of Pb-Sn alloys

The properties and behavior of metallic materials originate from their internal structure. Many properties, such as mechanical strength, corrosion and creep, depend on their microstructures. Alloys with desired properties can be achieved by tailoring the microstructure, either by controlling the composition or by processing. For example, the addition of elements such as selenium, copper or arsenic refines the grain structure of lead-antimony grids, while the addition of tin to lead-calcium grids increases their mechanical strength. Methods aimed to control the microstructure by physical processing include deforming the grids by a rolling operation or by casting the grids at different rates of cooling. A typical microstructure consists of a number of crystals or grains. These grains join at grain boundaries. Each grain is a single crystal with a periodic array of atoms. In the grain boundary regions, there is lack of atomic periodicity. The structures of these grain boundaries have a strong influence on the bulk (physical, mechanical and chemical) properties of the material. For instance, by increasing the area of grain boundaries, the grain size decreases and the mechanical strength increases. At elevated temperatures, however, grain boundaries enhance creep. (14)

For a gravity-cast grid with the composition Pb-0.06 wt. % Ca-0.6 wt. % Sn, the microstructure would consist of medium-sized grains, Figure 3.2 (a). If the level of calcium is increased in this alloy, but the same level of tin is unchanged, the grain size becomes much smaller, as shown in Figure 3.2 (b) for a grid of Pb-0.13 wt. % Ca-0.6 wt. % Sn. On the other hand, if the level of tin is increased, but the level of calcium is kept the same, then the grain size increases significantly. This is clear from Figure 3.2 (c) for a grid of Pb-0.06 wt. % Ca-1.5 wt. % Sn. Thus, the grain size increases with increasing tin content and decreasing calcium

content. It has also been found that the grain size depends on the Sn:Ca ratio. The microstructures of low-tin, high-calcium alloys will be fine grains with serrated grain boundaries. In contrast, the microstructures of high-tin, low-calcium alloys will be coarse grains with smooth (regular) grain boundaries. (14)

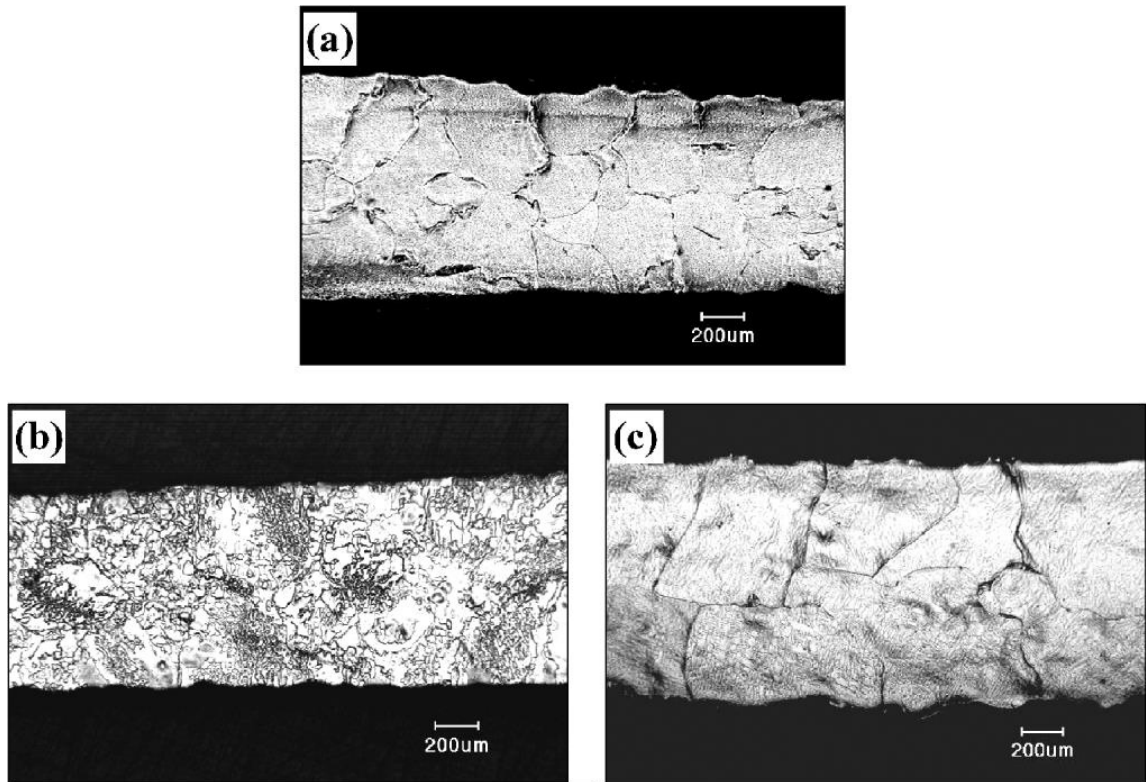


Fig. 3.2 Micrographs showing effects of calcium and tin additions on microstructure of: (a) Pb–0.06 wt. % Ca–0.6 wt. % Sn; (b) Pb–0.13 wt. % Ca–0.6 wt. % Sn; (c) Pb–0.06 wt. % Ca–1.5 wt. % Sn (14)

Typical microstructures observed at longitudinal sections along the castings length of Pb–1 wt% Sn and Pb–2.5 wt% Sn alloys are shown in Figures 3.3 and 3.4, respectively. The as-cast microstructures have a morphology which is exclusively cellular and constituted by a Pb-rich matrix (α -phase: solid solution of Sn in Pb) with a possible eutectic mixture in the intercellular regions. The Pb-rich cellular matrix is depicted by dark regions with the intercellular eutectic mixture being represented by light regions. A water-cooled mold increases the cooling rates near the casting/cooled surface (bottom) and a decreasing profile along the casting length (top) due to the increase in thermal resistance of the solidified shell with distance from the cooled surface, as reported in previous

articles (1; 2). This influence translates to the cellular growth, with smaller cell spacing near the bottom and larger ones close to the top of the casting, as shown by the microstructures of Figures 3.3 and 3.4.

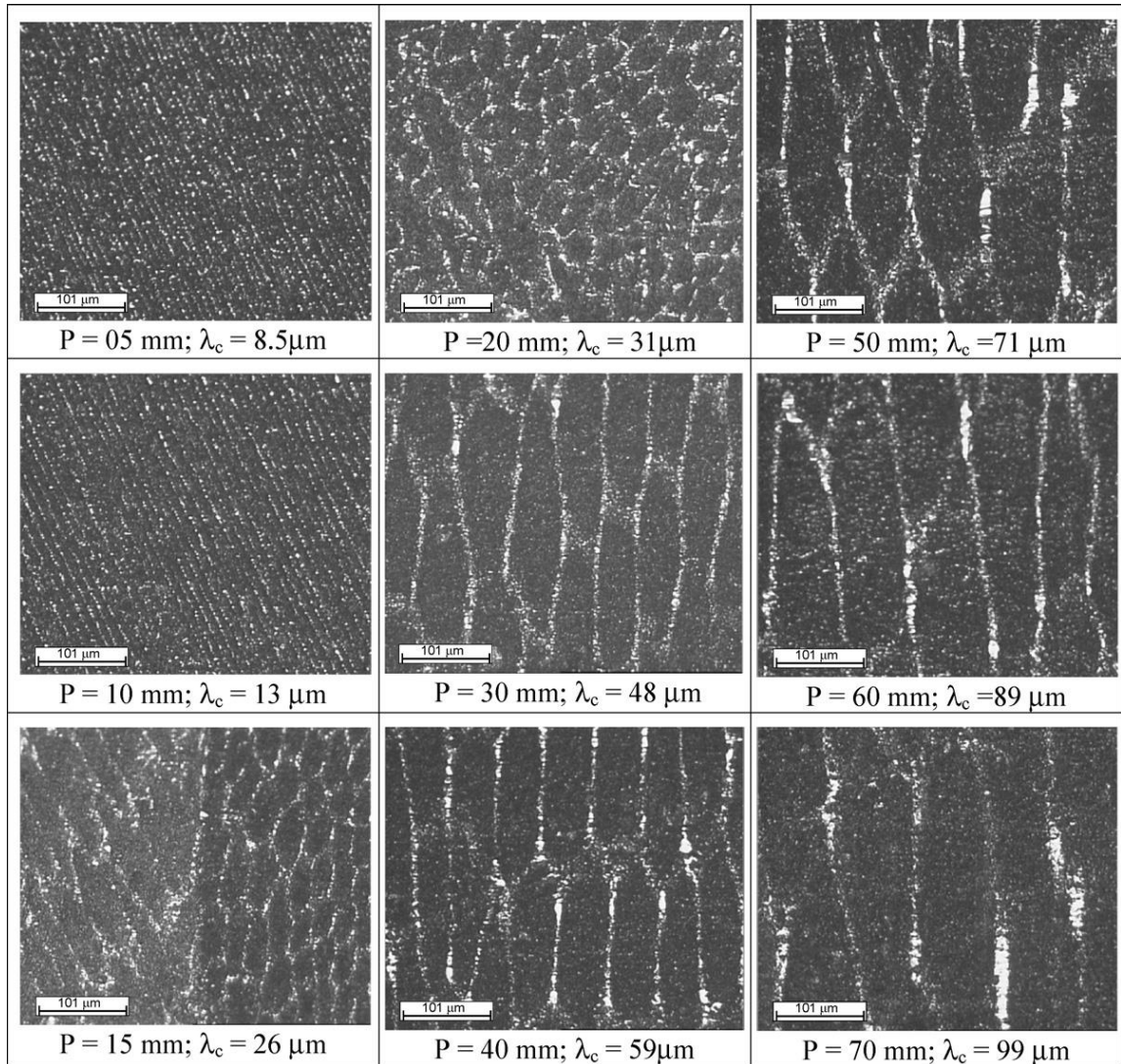


Fig. 3.3 Typical microstructures observed along at longitudinal sections and at different locations (5, 10, 15, 20, 30, 40, 50, 60 and 70mm) from the bottom of the casting for the Pb-1 wt% Sn alloy (optical magnification: 125x) (2)

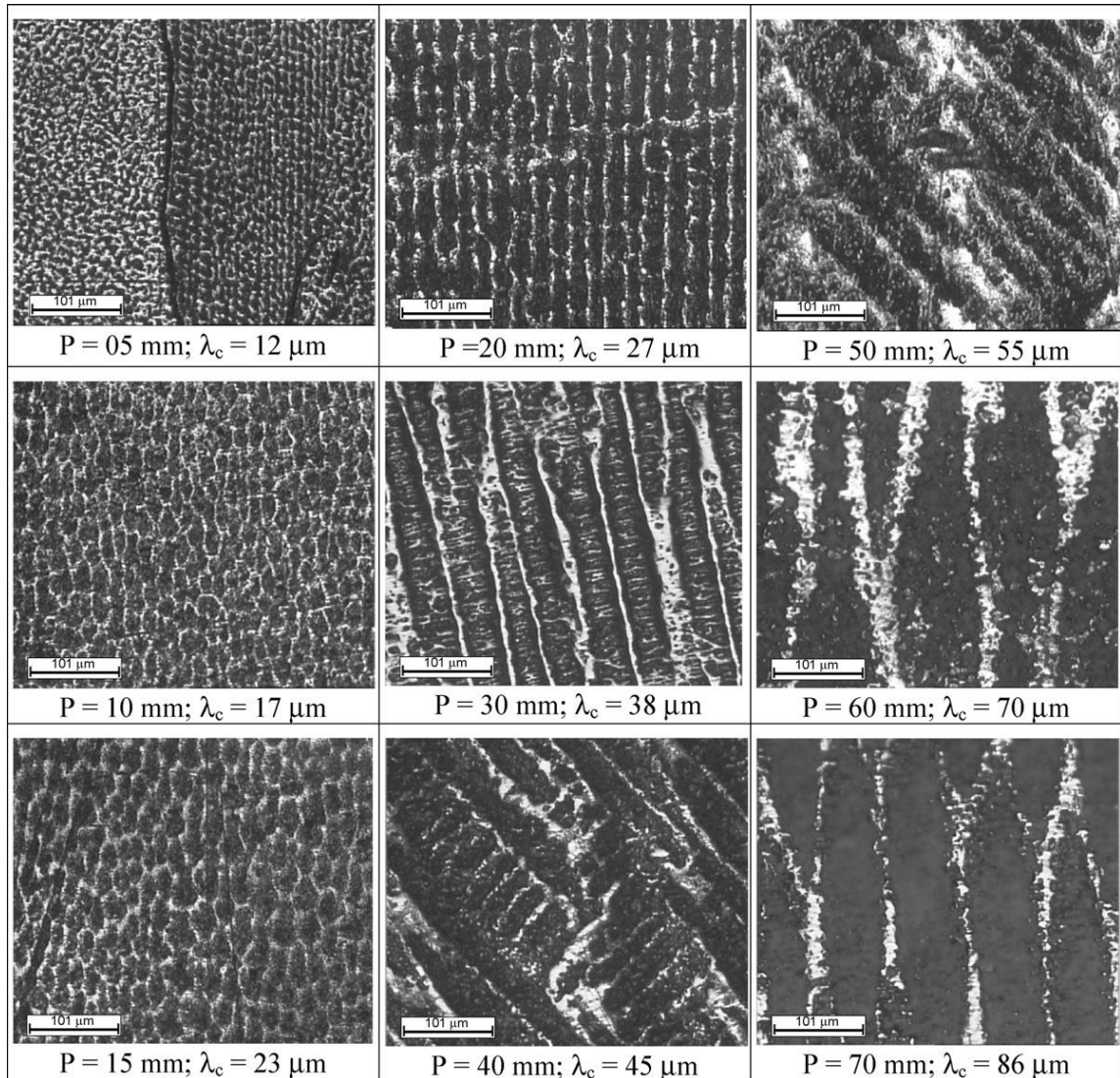


Fig. 3.4 Typical microstructures observed along at longitudinal sections and at different locations (5, 10, 15, 20, 30, 40, 50, 60 and 70mm) from the bottom of the casting for the Pb–2.5 wt% Sn alloy (optical magnification: 125x) (2)

3.3 Mechanical properties of Pb-Sn alloys

The grid must be of sufficient hardness and strength to support the mechanical and thermal strains incurred during the manufacturing process and throughout the subsequent service life of the battery; grid shape must be retained. The plate thickness increases during discharge and then decreases during re-charge, i.e., the plates ‘pulsate’ on battery cycling. This leads to deformation of the plate grids. Moreover, the positive plates are subject to corrosion. The

corrosion layer (CL) built of lead oxides have a 22-23% greater volume than that of unoxidized lead. Hence, it exerts mechanical stress on the metal and may deform the grid and impair its electrical contact with the active material. (13)

To be able to endure the stresses caused by the above phenomena, the plate grids should have sufficient hardness, high yield strength (YS), high creep strength and low elongation. Table 3.1 summarizes some of the specific mechanical grid characteristics, based on experimentally obtained data. (13)

Table 3.1 Required mechanical properties of lead-acid battery grids (13)

Grid Type	Brinell Hardness (kg mm ⁻²)	Tensile Strength (kg mm ⁻²)	Elongation (%)
EV batteries	12–15	4.5–6.5	4
SLI batteries	15–17	5–7	4

Lead-tin alloys with Sn content from 0.7 to 1.2 wt% Sn are used for casting grids for spirally wound and prismatic VRLA batteries for automotive, stationary and special purposes applications. Table 3.2 presents a summary of the mechanical properties of Pb-1.0 wt% Sn alloys with or without 0.06 wt% Ca. (13)

Table 3.2 Mechanical properties of Pb-1.0 wt% Sn alloys with or without 0.06 wt% Ca (13)

Alloy	Yield Strength (MPa)	Tensile Strength (MPa)	Elongation (%)	Creep Hours to Failure at 20.7 MPa
Pb–1.0 wt% Sn	4.5	12.3	55	0
Pb–1.0 wt% Sn –0.06 wt% Ca	46.2	55.2	24	800

The data presented in Table 3.2 suggests that the Pb-1.0 wt% Sn alloy has catastrophically poor mechanical properties. As this alloy is easy to bend, it is used for casting grids for spirally wound batteries. Handling of Pb-Sn grids in the process of plate manufacture requires special attention and automated machines are used for the purpose. However, Pb-Sn grids are characterized by high corrosion resistance and tin ions incorporated in the corrosion layer of the positive plates improve significantly its electro-conductivity as they catalyze the formation of PbO_n (1<n<2). (13)

A correlation has been found to exist between the conditions of thermal processing of the grids on casting and their mechanical properties and corrosion resistance. The thermal treatment parameters affect the sizes of the lead grains in the cast grids. The coarser grain structure of Pb-(1-2.5) wt% Sn alloys yields to an improved corrosion resistance due to the reduction of cellular boundaries. The alloy microstructure depends on the rate of melt cooling. An optimum cooling rate of between 1.5 and 0.8 °C s⁻¹ has been established for the Pb-1.0 wt% Sn alloy and between 0.6 and 0.5 °C s⁻¹ for the Pb-2.5 wt% Sn alloy. Such cooling rates yield cast grid microstructure that guarantees minimum corrosion and optimal mechanical properties. (13)

Figure 3.5 depicts the experimental results of ultimate tensile strength (σ_U) and yield strength ($\sigma_{y=0.2}$) as a function of cellular spacing (λ_c), for the Pb-1 and Pb-2.5 wt% Sn alloys. It can be seen for both alloys σ_U increases with decreasing cellular spacing. The segregated solute (tin) will lead to the formation of eutectic mixture in the intercellular region, which together with the cell boundary will constitute effective barriers to slip. The eutectic fraction in the intercellular region increases as the alloy Sn content is increased. (2)

The yield strength was shown to be constant with increasing the cellular spacing for the Pb-1 wt% Sn alloy, but this variable increases slightly with decreasing λ_c for the Pb-2.5 wt% Sn alloy. The cellular arrangement is not expected to affect significantly the elastic deformation, but it will affect the plastic deformation so that, the influence will depend on how deep in the plastic region the stress will be located and on the particular progress of plastic deformation of each Pb-Sn alloy. (2)

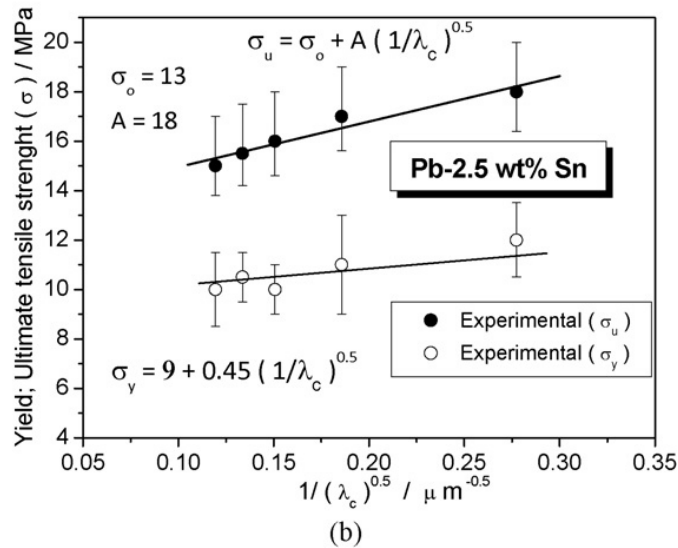
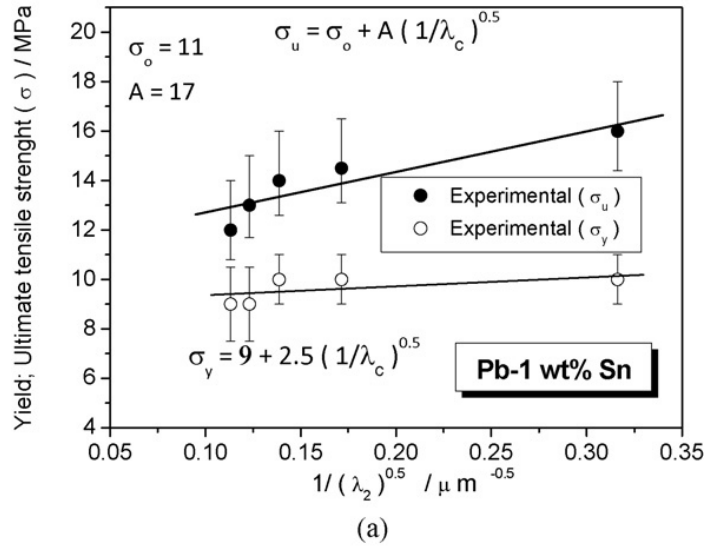


Fig. 3.5 Typical stress–strain curves as a function of cellular spacing: (a) Pb–1 wt% Sn and (b) Pb–2.5 wt% Sn alloys (2)

3.4 Pb-Sn alloys corrosion

Lead satisfactorily resists all but the most dilute strengths of sulfuric acid. It performs well with concentrations up to 95% at ambient temperatures, up to 85% at 220 °C, and up to 93% at 150 °C. Below a concentration of 5%, corrosion rates increase but remain in relatively low values. At lower H₂SO₄ concentrations, Pb-Sb alloys are recommended. Similar behavior patterns occur with chromic,

sulfurous, and phosphoric acids. The behavior of lead in sulfuric acid is shown in Figure 3.6. (17)

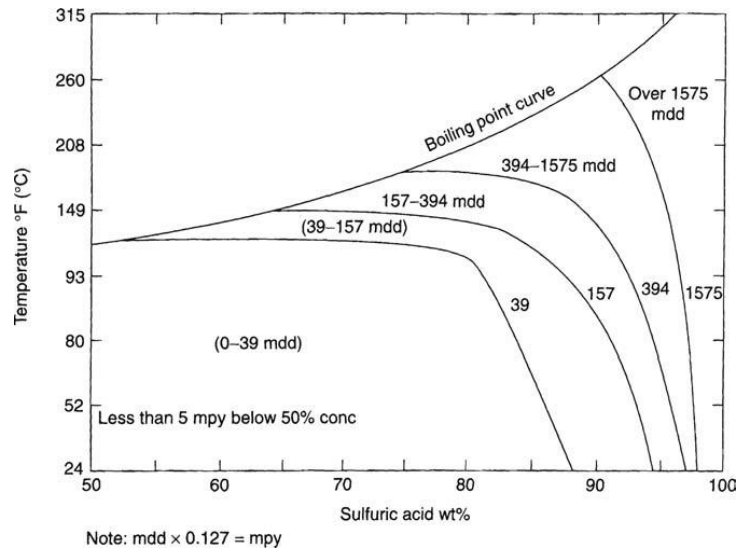


Fig. 3.6 Corrosion rate of lead in sulfuric acid (17)

In lead–calcium–tin alloys, corrosion occurs preferentially at the grain boundaries. Corrosion resistance improves with increasing grain size. Since the grain size is found to decrease with increasing calcium content, it can be expected that the corrosion rate will increase simultaneously. In addition, if the level of tin is increased, then the grain size increases, hence a reduction in the corrosion rate is experienced. However when the grain size becomes too large, the grids become susceptible to penetrating corrosion and may lead to catastrophic failure. (14)

Tin additions to pure lead have greatly diminished the problems experienced on cycling batteries with grids made from this metal. Small amounts of tin (0.3–0.6 wt. %) increase dramatically the charge-acceptance of pure lead. The beneficial effects of tin on passivation were demonstrated quite early. Tin additions to lead and lead alloys reduce the rate of bare-metal corrosion of grids to a significant degree. Pavlov demonstrated that tin doping of the PbO layer resulted in an increased photoelectric current, and therefore concluded that tin-containing corrosion layers were more conductive than those formed on pure lead. It has been suggested that complex semiconductor structures of SnO or SnO₂-doped PbO account for the increased conductivity of the corrosion layer. (7)

The addition of 0.6–0.7 wt. % Sn to a pure-lead positive grid can virtually eliminate the rapid loss in capacity displayed by VRLA batteries within the first 50

cycles. The results also show that the corrosion process changes from the formation of a continuous and uniform layer to a much more selective attack which penetrates into the grain boundaries. Despite the penetration, the corrosion rates are lower than that for pure lead. When tin is present at 0.6–0.7 wt. % in the alloy, doping of the corrosion layer at the grid-active material interface with SnO₂ inhibits, but does not eliminate, the formation of a passivation layer of PbSO₄ and/or α-PbO on the surface of the grid. (7)

Recently, there has been more definitive work on the addition of tin to lead and its effect on corrosion and passivation. In a series of experiments with 0.5–3.5 wt. % Sn added to lead, it was found that the passive layer which impedes electrical conduction through the grid-active material interface could be reduced or eliminated by the addition of sufficient tin. Below 0.8 wt. % Sn, the passive films have only ionic conductivity. The electrical conductivity increases rapidly beyond 0.8 wt. % Sn and reaches a plateau at 1.5 wt. % Sn. The investigation showed that the corrosion resistance of the alloy increases sharply as the tin content of the alloy increases. A minimum tin content of about 1.5 wt. % is required to ensure high conductivity of the corrosion layer and a minimum corrosion rate. It was found that tin inhibits the oxidation of Pb to Pb⁺², as predicted by an earlier model. (7)

By alloying lead with tin the oxidation of lead to PbO is inhibited, but intermediate compounds, PbO_x, can be formed. The corrosion product on pure lead is a semiconductor. Tin additions to the lead grid alloy transform the semiconducting corrosion layer of lead oxide into a lead–tin oxide layer, which is highly conductive. The tin content of the passive film is greatly increased i.e., from 3 wt. % for an alloy of 0.5 wt. % Sn to 44 wt. % for an alloy of 3.5 wt. % Sn. Measurement of the resistance of the grid-active material interface upon cycling in actual cells has shown that antimony or tin additions to grids improve the conductivity of the corrosion layer. (7)

At high pH values, lead is oxidized to Pb(OH)₂ in a first step, and tin is oxidized, first to SnO, and subsequently to SnO₂. The Pb(OH)₂ may be reduced by SnO back to lead with consequent formation of SnO₂, in a simple redox procedure. In this reaction, the PbO layer becomes thinner and more enriched with SnO₂. Significant conductivity of the grid-active material interface requires a concentration of tin of 10 wt. % or higher in the corrosion product. (3)

The results indicate that corrosion layer thickness, structure and composition are influenced by positive active material type and grid alloy. Corrosion layer thickness is related to the number of cycles. However, positive active material and grid type appear to be the more influential factors. (18)

Porosity in the corrosion layer was greater in electrodes with sulphated active materials. These layers were also significantly thicker than their non sulphated equivalent and it is believed that this is a result of an increased amount of oxygen reaching the grid/corrosion layer interface through the network of pores and cracks. (18)

Tin in the alloy decreases oxygen and hydrogen gassing at the positive and negative electrodes, respectively. Tin has also been found to decrease the thickness of the passivation PbO layer. (14)

Coarser cells tend to improve the corrosion resistance of both Pb-1 wt% Sn and Pb-2.5 wt% Sn alloys mainly due to the reduction of cellular boundaries. (2)

The experimental EIS diagrams, impedance parameters, anodic potentiodynamic polarization curves and the fitted equivalent circuit parameters have shown that coarse cellular structures tend to yield higher corrosion resistance than fine cellular morphologies for an as-cast Pb-1%Sn alloy. Such trend is associated with the reduction of cellular boundaries of coarse cellular arrays when compared with finer cells, since the boundary has proved to be more susceptible to the corrosion action. These results indicate that the control of as-cast cellular microstructures, by manipulating solidification processing variables permitting the control of cooling rate, can be used as an alternative way to produce as-cast components of Pb-Sn dilute alloys for battery components with improved corrosion resistance. (1)

Investigations have been conducted that using Pb-2 wt% Sn electrodes (in the form of straps 6 cm long, 0.8 cm wide and 0.15 cm thick) partly inserted into AGM soaked in H₂SO₄ or (H₂SO₄ + Na₂SO₄) solutions. Figure 3.7 shows the measured weight losses of the electrodes with time of stay in oxygen atmosphere at 50 °C. Additions of Na₂SO₄ to the sulfuric acid solution lead to a seven-fold increase of the corrosion rate. This is probably due to the increased solubility of PbSO₄ in the presence of Na⁺ ions in the solution and hence to the modified structure of the corrosion layer. Figure 3.8 (a) shows the corrosion transients for electrodes cast from Pb-2.0 wt% Sn or Pb-2.0 wt% Sn-0.03 wt% Se alloys and partly inserted in AGM soaked in H₂SO₄ solution. The transients obtained for electrodes immersed in AGM soaked in H₂SO₄ + Na₂SO₄ solution are presented in Figure 3.8 (b). (13)

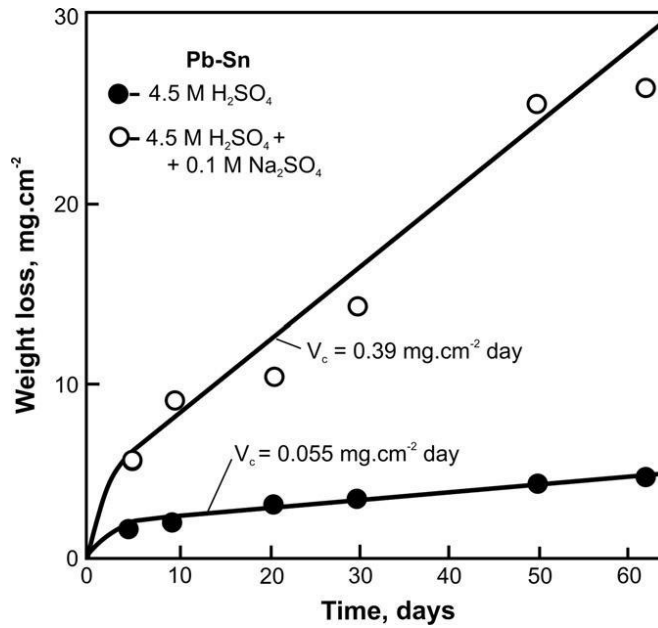


Fig. 3.7 Weight losses of Pb-2.0 wt% Sn electrodes with time of stay at 50 °C in oxygen atmosphere (13)

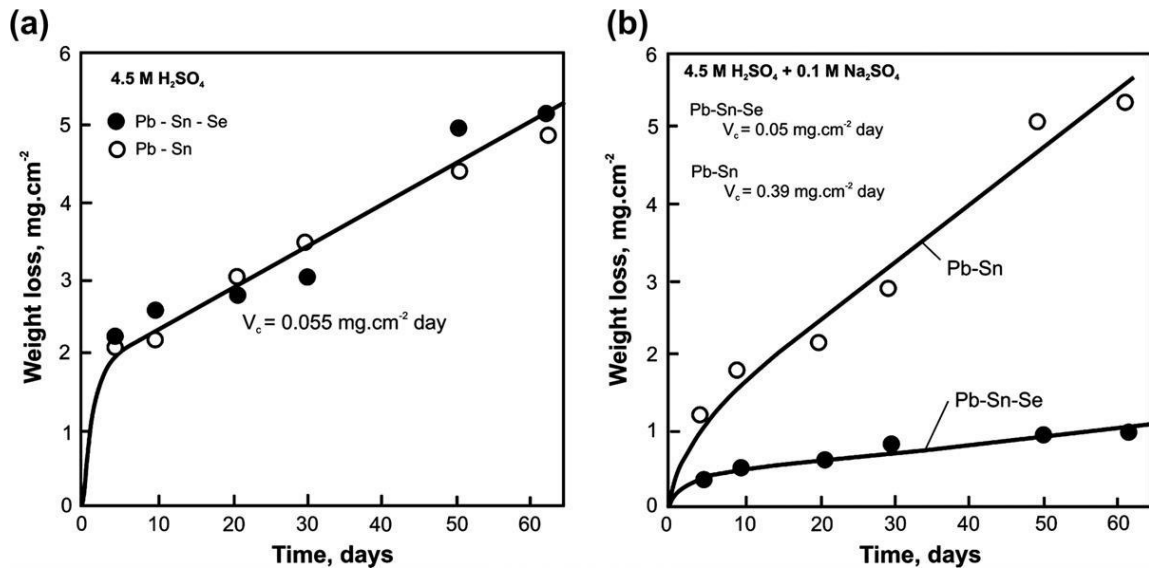


Fig. 3.8 Corrosion transients for Pb-2.0 wt% Sn and Pb-2.0 wt% Sn-0.03 wt% Se electrodes partly inserted in AGM soaked in (a) H₂SO₄ and (b) H₂SO₄ + Na₂SO₄ solution (13)

Additions of selenium to the electrode alloy do not have a notable effect on the rate of corrosion, when the Pb-2.0 wt% Sn electrodes are immersed in H₂SO₄ solution. The situation is different, however, when the AGM is soaked in H₂SO₄ +

Na_2SO_4 solution. In this case, Se strongly reduces the corrosion rate of Pb-2.0 wt% Sn alloys. Hence, the detrimental effect of Na_2SO_4 addition on the corrosion rate of Pb-2.0 wt% Sn alloys is suppressed by adding Se to the alloy. Figure 3.8 indicates that the corrosion rate of Pb-Sn-Se alloys is about eight times lower than that of Pb-Sn alloys in $\text{H}_2\text{SO}_4 + \text{Na}_2\text{SO}_4$ solution. (13)

It has also been established that Pb-Sn alloys with Sn content below 1.0 wt% are subject to higher corrosion rates. Selenium suppresses this effect, too, in alloys containing 0.6 wt% Sn. Selenium has an anti-corrosion effect and acts as grain refiner in Pb-Sn alloys, reducing also the size of PbSO_4 crystals and facilitating their nucleation. (13)

CHAPTER 4 EXPERIMENTAL PROCEDURE

4.1 Introduction

For the development of the experimental procedure a sample of Pb-Sn alloy casted strip was selected with a composition of Sn <1.0 wt. %. This alloy was produced following standard processing conditions. The exact composition of the master alloy is not given in this work because it is an intellectual property of the company where this study was developed.

The samples were cut to strips of 1.7 x 20 cm to apply different thermal treatments, then specimens were shaped to a dog bone morphology for tension measurements and finally mounted into special devices for corrosion rate measurements.

To understand the microstructural behavior of the Pb-Sn alloy under different conditions of temperature and cooling (thermal treatment) and how these changes affect grain size and the corrosion rate under different acid concentrations, a design of experiments (DOE) was created and is discussed accordingly.

4.2 Experimental plan

The schematic representation of the work plan is given in Figure 4.1.

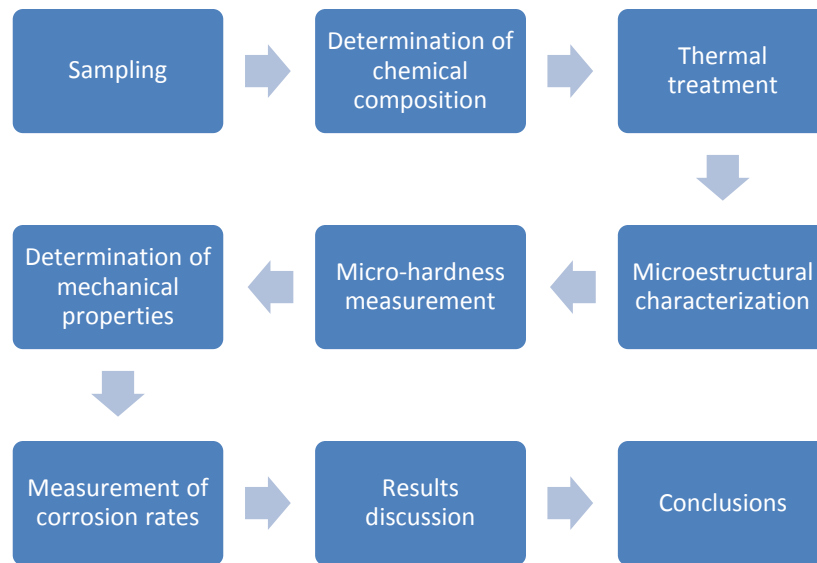


Fig. 4.1 Experimental flow chart

4.3 Samples

A master sample was of 200 x 20 cm was collected during a standard run of a strip casting machine. This sample was subjected at the standard cooling period of 8 hours. Once cooled, samples were cut to strips of 1.7 x 20 cm.



Fig. 4.2 Cutting samples to strips

It is also worth mentioning that the strips were machined to a dog bone shape s according to the ASTM-E345 Standard Test Methods of Tension Testing of Metallic Foil (19). During the time that the samples were not manipulated either

for heat treating or measurements, the samples were stored at a $-18\text{ }^{\circ}\text{C}$ temperature to prevent further microstructural changes due to aging of the alloy.

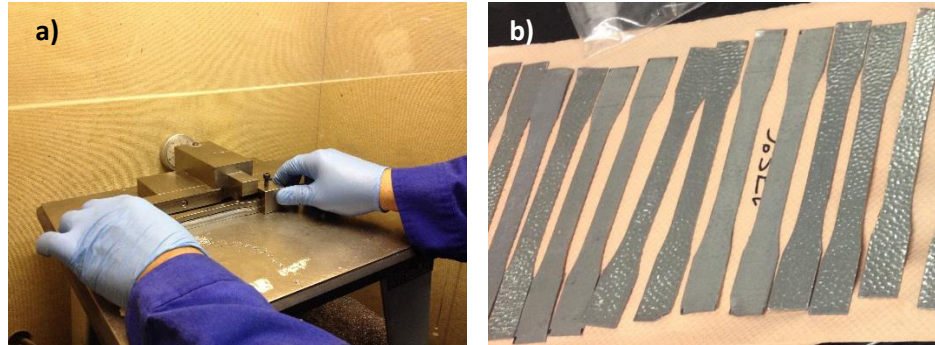


Fig. 4.3 (a) Sample machining to “dog bone” shape; (b) “dog bone” shaped samples

4.4 Determination of the chemical composition

For the determination of the chemical composition of the Pb-Sn alloy an arch and spark spectrometer model ARL-4460 Mettler Toledo was used. Chemical composition of the alloy was validated by means of determining the weight content of Pb and Sn according to company standards.



Fig. 4.4 Mettler-Toledo arch and spark spectrometer

4.5 Heat treatment of the alloy

The heat treatments schedule at which the alloy was subjected is shown in Figure 4.5.

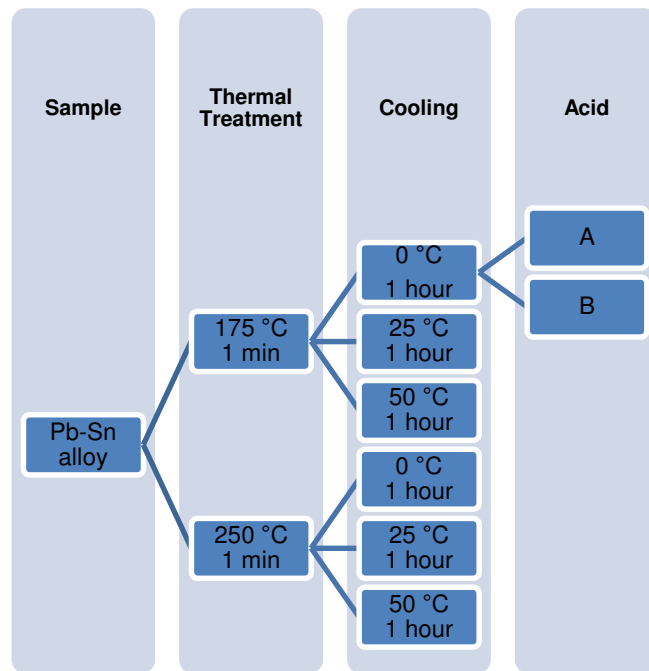


Fig. 4.5 Diagram of thermal treatments for Pb-Sn binary alloys

The heat treatments were conducted using in all cases the maximum temperatures either 175 or 250°C remaining at these values for 1 minute. Then, the samples were cooled to three different temperatures almost at the same cooling rate and remaining 60 minutes as shown in Figures 4.6 and 4.7.

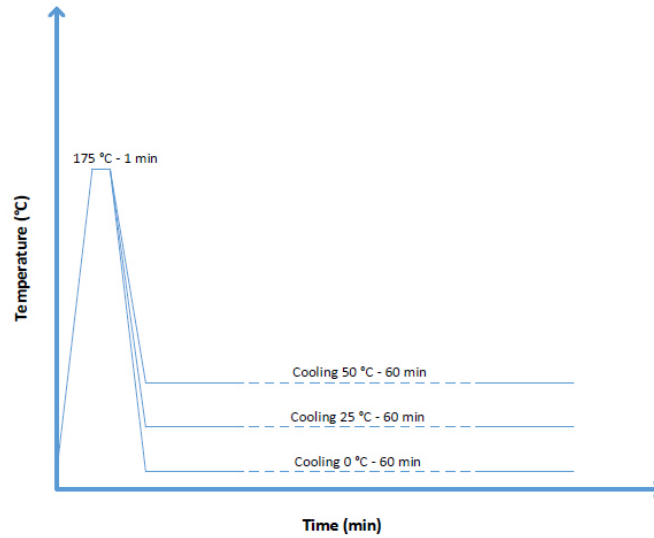


Fig. 4.6 Thermal treatments for Pb-Sn binary alloys at 175 °C with 3 different cooling temperatures

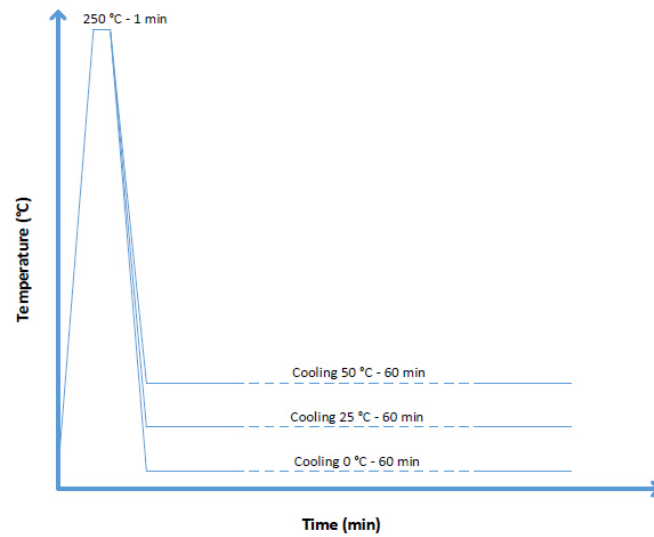


Fig. 4.7 Thermal treatments for Pb-Sn binary alloys at 250 °C with 3 different cooling temperatures

All heat treatments were performed in the facilities of Johnson Controls Global Laboratory, using a state of art mechanical convection furnace.



Fig. 4.8 Mechanical Convection Oven 625 FREAS used for thermal treatments

4.6 Microstructural characterization

The metallographic analysis of the samples was carried out following standard metallographic procedures grinding one face of the specimens using various grades of abrasive silicon carbide (SiC) paper, followed by a final polishing using diamond pastes of 3 and 1 μm on hard and soft polishing cloths respectively to produce a scratch-free mirror finish.

After the polishing procedure, the samples were etched by immersion in a solution of 10 ml of glycerin, 10 ml of hydrogen peroxide and 20 ml of concentrated acetic acid for 5 seconds, then the samples are washed and dried.



Fig. 4.9 Variable Speed Grinder-Polisher EcoMet 3000 BUEHLER used for sample polishing

After etching, the samples were inspected using a MCA UNITRON MODZST microscope, and images were taken using a digital camera. The analysis of the images was conducted using the software Image-Pro Plus Version 7.0.0.591.



Fig. 4.10 MCA UNITRON MODZST microscope

4.7 Micro-hardness measurements

After heat treating, samples of each condition were used to determine the Vickers micro-hardness values using loads of 0.2 kg for 15 seconds. These measurements were conducted in a Wilson Instron Tukon 2100 (Figure 4.11).



Fig. 4.11 Micro-durometer Wilson Instron Tukon 2100 for micro-hardness measuring

4.8 Determination of mechanical properties

For the determination of mechanical properties precisely, the tensile strength of the alloys was performed using 5 specimens of each heat treating condition, the test was performed at a strain rate of 10 mm/min speed according to the ASTM-E345 Standard Test Methods of Tension Testing of Metallic Foil (19). An extensometer was used to improve the accuracy of tests which were developed in a MTS Sintech 1/G universal machine (Figure 4.12).

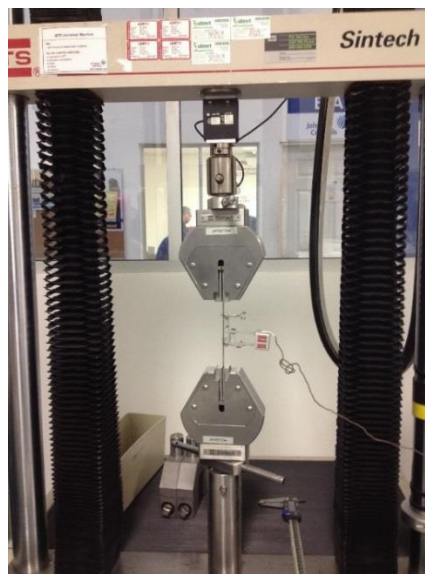


Fig. 4.12 Universal testing machine MTS Sintech 1/G

4.9 Corrosion rate of the specimens

The corrosion rates of the specimens were measured in 6 samples for all the different heat treating conditions, the samples were exposed to two different acid concentrations: A and B, where concentration of acid B is higher than A. As in the case of the chemical composition of the alloy, the concentration of the acids nor the composition cannot be given in this document. To build work electrodes, each sample was mounted in acrylic resin and then grinded using various stages of abrasive silicon carbide (SiC) papers followed by a final polishing using diamond pastes of 3 and 1 μm on hard and soft polishing cloths respectively to produce a scratch-free mirror finish as it is shown on Figure 4.13.

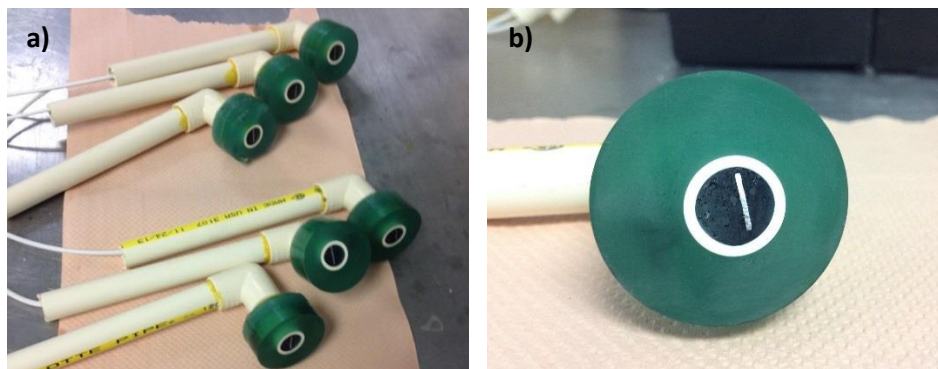


Fig. 4.13 (a) Samples mounted as work electrodes; (b) Exposed surface for corrosion rate measuring

Once the samples were mounted as electrodes, the surface area exposed was measured of the software Image-Pro Plus Version 7.0.0.591 as it is shown on Figure 4.14.

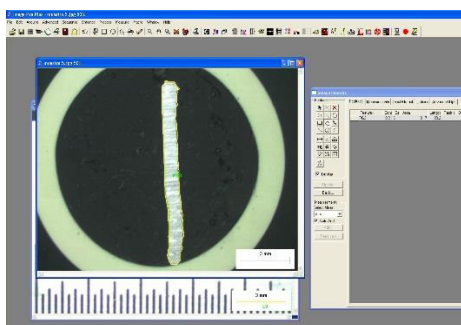


Fig. 4.14 Surface area measuring with software Image-Pro Plus

The electrical circuit was made with the alloy as working electrodes, using a $\text{Ag}/\text{Ag}_2\text{SO}_4$ electrode as a reference electrode and a Pt mesh electrode with known area was used as a counter electrode. The circuit arrangements are shown on Figure 4.15.



Fig. 4.15 (a) Work, counter electrode and reference electrodes; (b) Samples arrangement with Potentiostat/Galvanostat

For the corrosion measurements, a Princeton Applied Research/EG&G Model 273 Potentiostat/Galvanostat was used, the default Tafel template performed a scan starting at -250 mV vs. OC, and scans to +250 mV vs. OC at a scan rate of 0.166 mV/s.

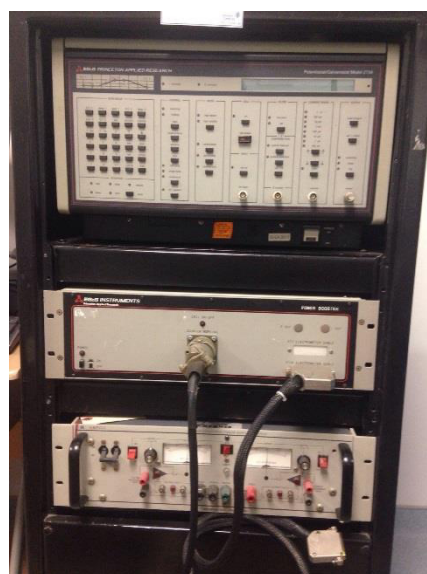


Fig. 4.16 Princeton Applied Research / EG&G Model 273 Potentiostat/Galvanostat

CHAPTER 5 RESULTS AND DISCUSSIONS

In this chapter the results obtained from this investigation are presented, analyzed and discussed. Firstly, the effect of the heat treatments on the microstructural changes experienced by the samples and then, the results on the relations among microstructure, grain size and corrosion behavior of the samples exposed to two different acid concentrations.

Then, a statistical analysis of the data given by the Design of Experiments (DOE) is presented, trying to obtain a mathematical expression that can explain the behavior of the corrosion rate on the Pb-Sn alloys under the given conditions.

5.1 Results

5.1.1 Chemical composition of the alloys

Given that previous works with Pb-Sn alloys studied the range of composition 1.0-2.5 wt. % Sn, compositions lower than <1.0 wt. % Sn are the subject of this study. The results from the spark spectrometer confirmed that the alloy composition was indeed within the composition expected.

5.1.2 Microstructural characterization after thermal treatments

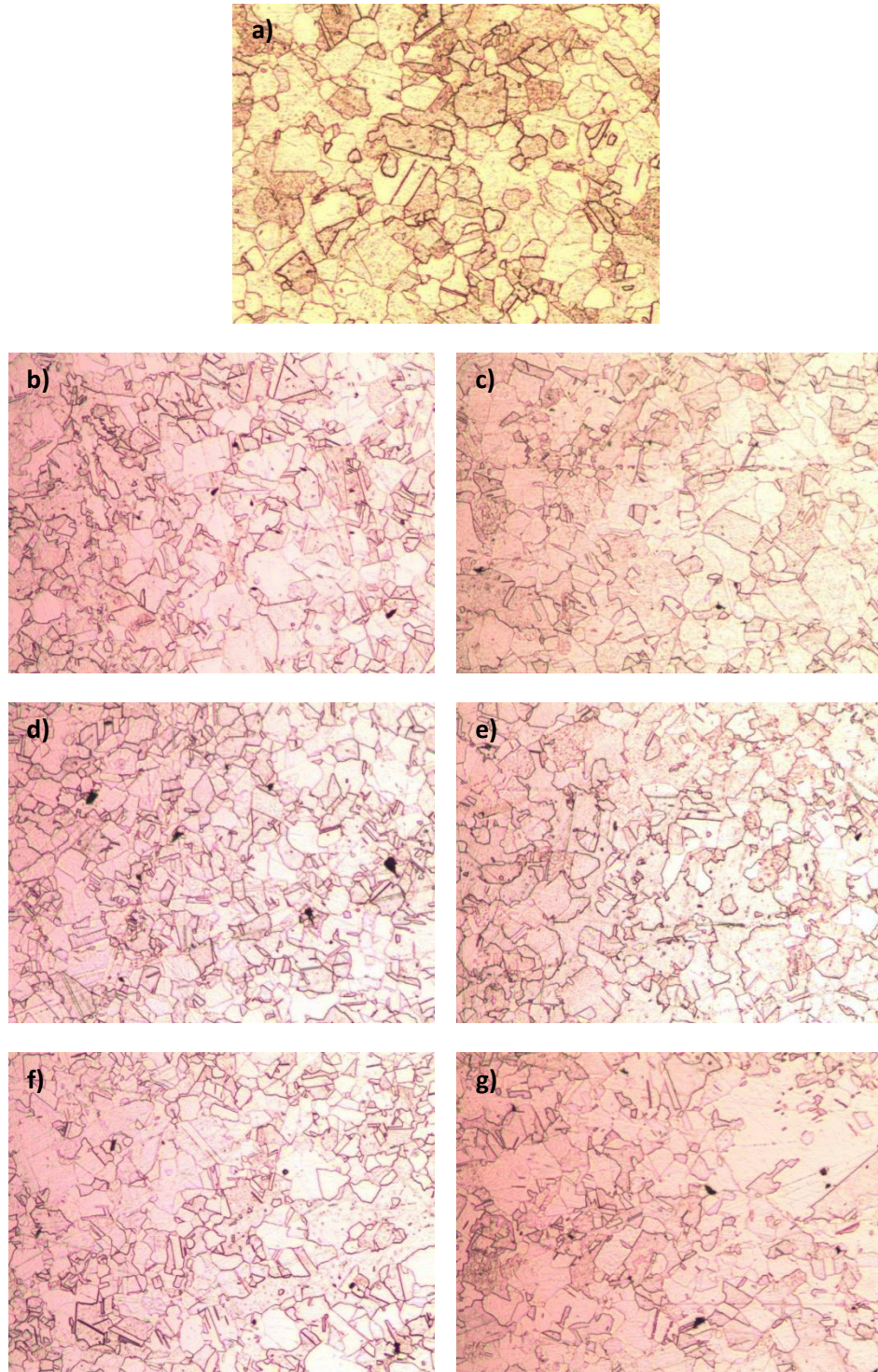


Fig. 5.1 Microstructure of Pb-Sn alloy at 100x (a) initial; (b) TT 175 °C cooling 0°C; (c) TT 250 °C cooling 0°C; (d) TT 175 °C cooling 25°C; (e) TT 250 °C cooling 25°C; (f) TT 175 °C cooling 50°C; (g) TT 250 °C cooling 50°C

Figures 5.1 (a) to (f) give the microstructures of Pb-Sn alloys under the different heat treating conditions. Figure 5.1 (a) gives the microstructure of the master alloy in the control condition, where coarse grains and annealing twins can be appreciated. In addition, Figures 5.1 (b) and (c) contain similar microstructural features as to those found in control specimen, even though they were heat treated with different conditions. Contrarily to the figures previously analyzed, in Figures 5.1 (d) and (e) smaller grain sizes than those observed in the control samples can be appreciated. Finally, Figures 5.1 (g) and (f) resulted with bigger grain size than those present in the control sample.

Table 5.1 Grain size results for each thermal treatment

Thermal Treatment Temp. °C	Cooling Temp. °C	Grain size
175	0	8.01
175	25	7.38
175	50	7.92
250	0	5.40
250	25	7.50
250	50	7.59

From the analysis of the microstructure and the grain sizes that results from heat treatments (shown in Table 5.1), it is clear that there is an effect of the heat treating route on the microstructural evolution of the samples being the cooling temperature, the variable that seems to control the grain sizes. This behavior totally agrees with the investigation of Rossi (20) where it is mentioned that the cooling rate and temperatures of lead alloys affect their ageing behavior.

For the samples that were cooled to 50 °C, a greater grain size was obtained if compared to the grain size of the control sample and the samples cooled to 0°C. This is expected if it is considered that this temperature is suitable as to promote diffusion processes that could favor grain growth, sometimes in abnormal ways as it shown in Figure 5.1 (g).

As it was also expected, cooling to 25 °C promoted smaller grain sizes if compared to those obtained after cooling to 50°C. Definitely, the energy for grain growth was not enough as to promote the growth of grains with sizes similar to those observed at 50°C providing that the temperature at which the samples

remained for an hour after high temperature exposure was lower than 50°C. This could be explained in terms of the activation energy for grain growth which for sure included a higher value for this process to occur.

In the other hand, microstructure of samples cooled at 0 °C remain practically the same than at the control sample, this could be explain due that tin ions diffusion is much lower at that temperature rather than at 25 or 50 °C.

5.1.3 Micro-hardness measurement

For the Vickers micro-hardness measurements, loads of 0.2 kg for 15 seconds were used producing a rhombohedra like indentation in the sample, both vertices were measured according to Figure 5.2.

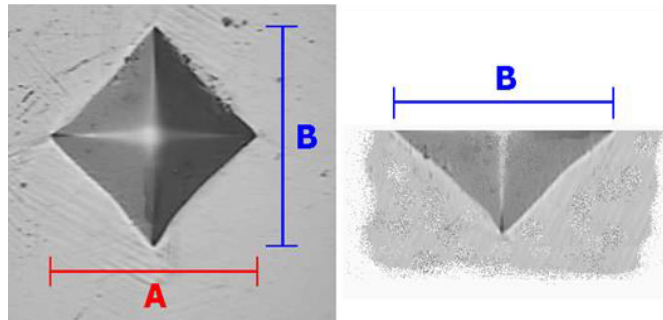


Fig. 5.2 Measurements for micro-hardness

The final result of micro-hardness is given by the formula:

$$Vickers\ micro - hardness = \frac{(1854.3677)(200)}{\left(\frac{A+B}{2}\right)^2} \quad (5.1)$$

Where A is the distance of the horizontal vertices and B is the distance of the vertical vertices, both in μm .

According to results given on Table 5.2, there is no significant difference among the results of different heat treatments, probably because the time or the temperature of the heat treatments was not enough as to promote migration of Sn to the grain boundaries and with this, produce increments in the hardness of the alloy. This behavior also agrees with the investigation of Rossi (20) where no

considerable difference in hardness values were obtain for similar cooling rates as the ones used in this investigation even though the alloys here used represent a different metallic system.

Table 5.2 Micro-hardness results for each thermal treatment

Sample	Initial	TTT 175 °C Cooling 0 °C	TTT 175 °C Cooling 25 °C	TTT 175 °C Cooling 50 °C	TTT 250 °C Cooling 0 °C	TTT 250 °C Cooling 25 °C	TTT 250 °C Cooling 50 °C
1	6	6	5	5	5	5	5
2	5	5	5	5	6	6	5
3	5	6	6	6	5	6	5
4	5	6	5	5	5	6	6
5	5	5	6	5	5	5	5
Average	5.2	5.6	5.4	5.2	5.2	5.6	5.2

5.1.4 Determination of mechanical properties

The analysis of the results given on Table 5.3 that relate the mechanical properties of alloys for different heat treatment routes, it is possible to identify the following features. The alloys exposed to 175 °C during heat treatment experience, in most cases, higher results of peak stress (MPa) than those exposed to 250 °C. It is also worth mentioning that a similar behavior was found in the strain at break (%). The opposite behavior was found during the analysis of the elastic modulus (MPa) of the samples, where higher values were found for the samples treated at 250 °C.

Regarding the values of strain at yield (%) there was no significant difference among the results of the different heat treatments, but in the stress at yield (MPa) the samples treated at 250 °C showed average values that are 4% lower than samples treated at 175 °C.

Table 5.3 Mechanical properties of the samples for each thermal treatment

Thermal Treatment Temp. °C	Cooling Temp. °C	Peak Stress MPa	Strain At Break %	Modulus MPa	Strain At Yield %	Stress At Yield MPa
175	0	14.9255	31.9840	2,246.60	14.1148	13.7109
175	25	15.1170	33.5600	5,112.40	14.7170	13.8457
175	50	14.6147	32.0032	4,968.40	14.4978	13.4697
250	0	14.4044	31.3886	5,453.40	14.8606	13.2910
250	25	14.0315	27.5334	6,768.20	14.0098	13.0675
250	50	14.1024	30.2836	3,193.80	14.5700	13.0782

Figure 5.3 shows the strain (%) vs stress (MPa) relationship for samples treated at 175 °C and the master sample. Figure 5.4 shows the strain (%) vs stress (MPa) relationship for samples heat treated at 250 °C and the master sample.

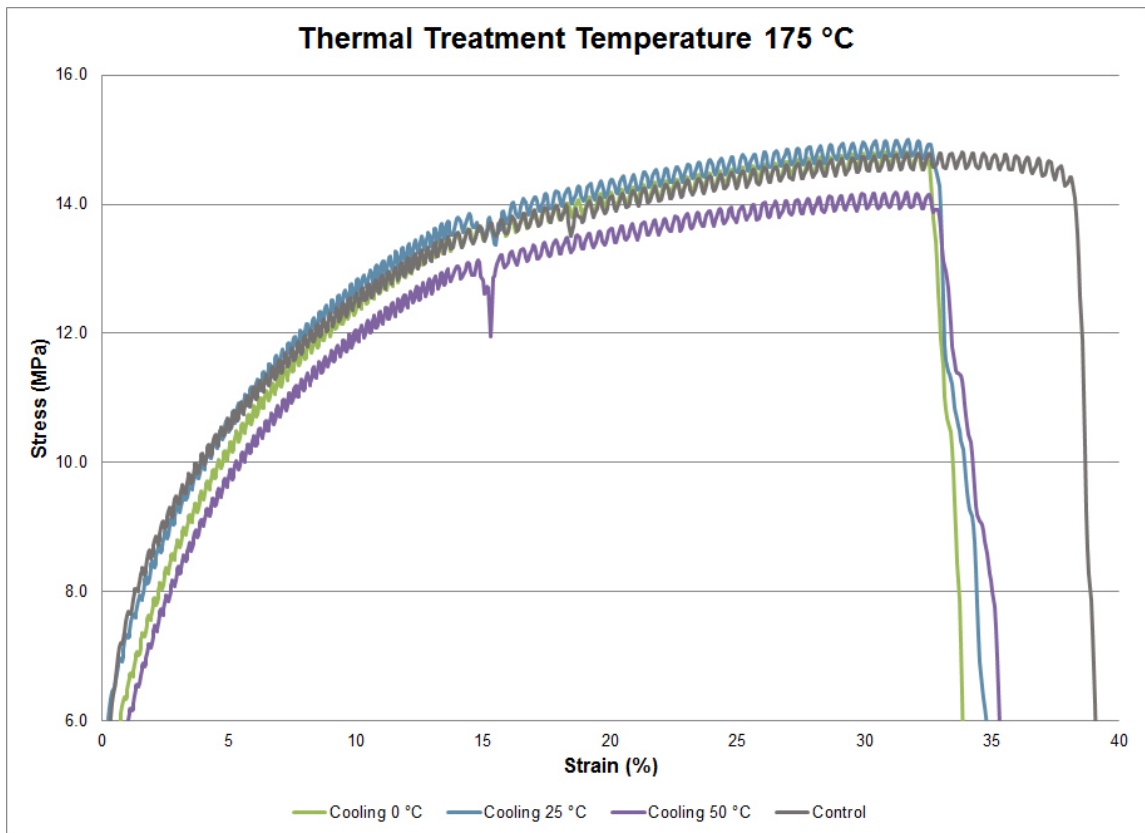


Fig. 5.3 Mechanical properties of samples heat treated at 175 °C

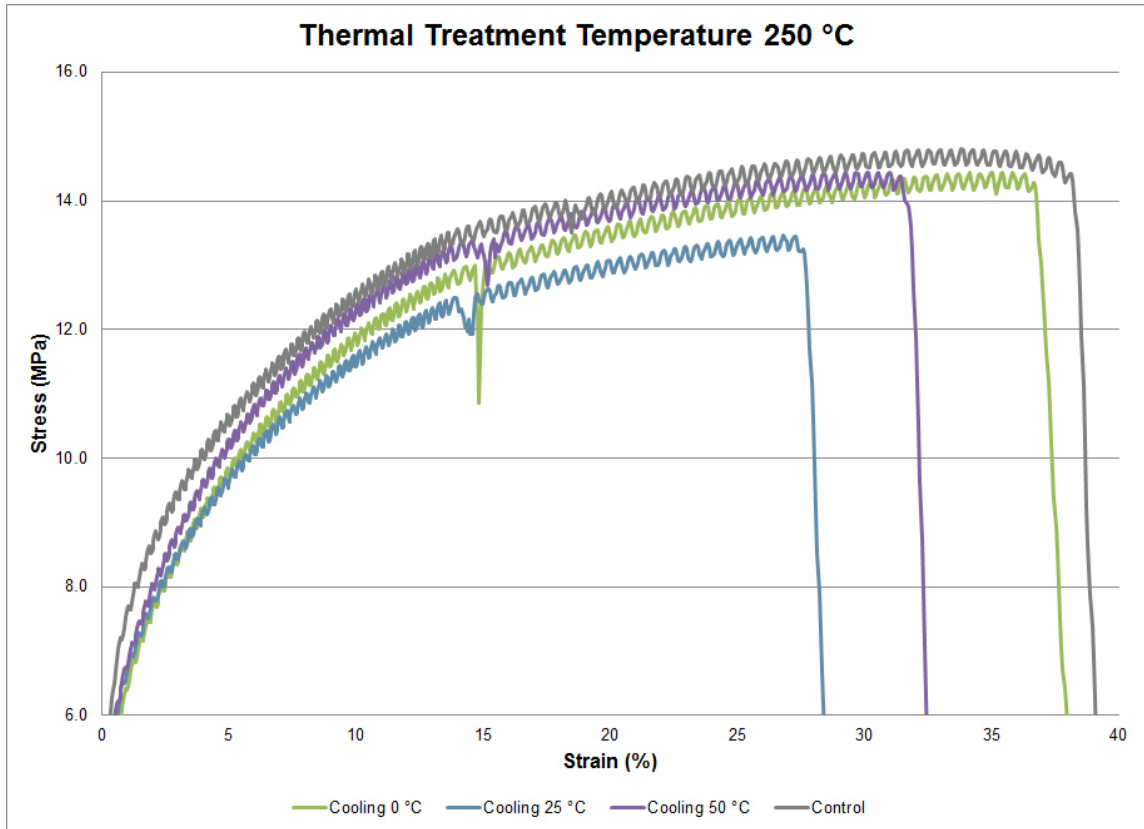


Fig. 5.4 Mechanical properties of samples heat treated at 250 °C

5.1.5 Measurement of the corrosion rates

The corrosion rates of the samples are shown at Table 5.4. In this table, it is possible to appreciate that corrosion rates (given in millimeters per year) for samples that were treated at 250 °C, are considerably higher than the corrosion rates that those samples that were treated at 175 °C. This is probably given by the difference in the grain size, it can be said that coarse cellular structures tend to yield higher corrosion resistance than fine cellular morphology which agrees with the behavior of alloys with higher weight content of Sn reported in previous works. Such considerations are associated with the reduction of cellular boundaries of coarse cellular arrays when compared with finer cells, since the boundary has proved to be more susceptible to the corrosion action. (21; 1; 13)

In addition, the samples that were cooled at 25 °C, regardless of the maximum temperature present in average, the highest corrosion rates, followed

by samples cooled at 50 °C and 0 °C which experience the lowest values of corrosion rates.

Furthermore, as it was expected, average corrosion rates of samples that were exposed to a lower concentration of acid (acid concentration A) experienced higher corrosion rates if compared with the samples that were exposed to a higher acid concentration (acid concentration B). This is given because, the lower the acid concentration is, the fastest the passive layer is dissolved, therefore, the highest the corrosion rate. The effect of acid concentration in Pb-Sn alloys was not compared with similar studies of Osório (1; 2; 21) given that investigations employed only one acid concentration.

Table 5.4 Corrosion rate results for each thermal treatment and acid concentration

Thermal Treatment Temp. °C	Cooling Temp. °C	Acid Conc.	Corrosion rate mry	Grain size
175	0	A	38.27	8.01
175	0	B	20.24	
175	25	A	44.28	7.38
175	25	B	19.43	
175	50	A	34.19	7.92
175	50	B	14.96	
250	0	A	28.81	5.40
250	0	B	51.66	
250	25	A	448.6	7.50
250	25	B	247.6	
250	50	A	346.1	7.59
250	50	B	224.45	

Minitab is a software widely used for the analysis of statistical data, in this case of this study, generates a model named “design of experiments” which helps to understand relationship among several variables, such as thermal treatment temperature, cooling temperature and acid concentration, also, the relationship of those variables in the result, in this case, corrosion rate.

With the aid of Minitab software the analysis of the most important effects that control the degradation of the samples is shown in Figure 5.5. This analysis suggests that the factor which causes more impact on the corrosion rate of the alloys is the temperature at which the heat treatments were developed. According

to this, the greater the temperature of heat treatment ($^{\circ}\text{C}$) is, the greater the corrosion rate (mpy) will be. This can be explained based on the impact that temperature of heat treatment exerts in the grain size.

The relationship between the corrosion rate and the cooling temperature, is not a linear one; and the corrosion rate increased when cooling temperature increased from 0°C to 25°C , and then decreased again when samples were cooled at 50°C . This behavior agrees with previous work from Razaei (22) where it is mentioned that at a lower cooling rate of lead alloy casting, impurities present in the lead alloys (e.g., antimony) penetrate to the interior of the mold and their concentrations decrease at the surface of the electrodes, therefore, these electrodes show different electrochemical behavior.

Finally as it was expected, for all the tests, the lower the acid concentration is, the higher the corrosion rate will be.

According to the statistical analysis developed by the software, the lowest corrosion rate should be found with the following combination of factors: 175°C of thermal treatment temperature, 0°C of cooling temperature and acid concentration B. This was almost true in the experimental data, except that the lowest corrosion rate has 50°C of cooling temperature.

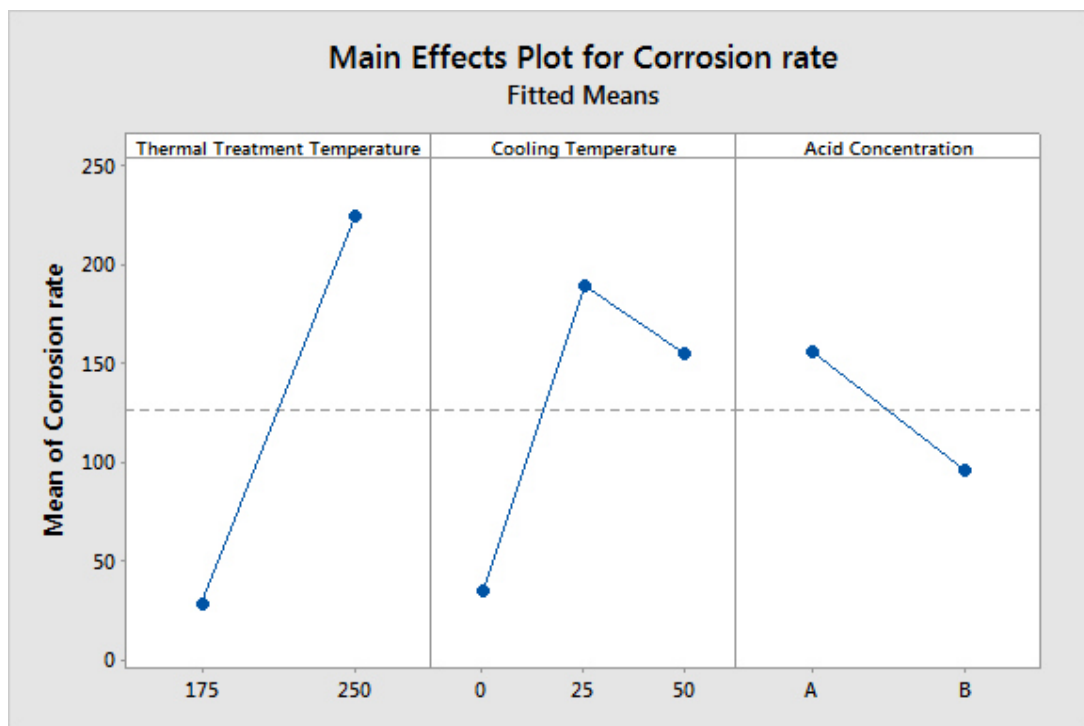


Fig. 5.5 Main effects plot for corrosion rate

Based on a regression analysis of the results from the design of experiments, it is possible to conclude that there is a regression equation that explains 86.4% of the results. In the regression equation given on Figure 5.6 and Equation 5.1, it is possible to appreciate that the biggest coefficient is for the acid concentration, this means that it has the strongest effect on corrosion rate. Then, the grain size is the next biggest coefficient which represent the second most important variable.

$$\text{Corrosion rate (mpy)} = -2,648 + 3.73 \text{ Thermal Treatment Temperature} - 1,077 \text{ Acid Concentration} - 60.7 \text{ Grain Size}^2 + 915 \text{ Grain size} \quad (5.1)$$

Regression Analysis: Corrosion ra versus Thermal Trea, Acid Concent, ...

The regression equation is

Corrosion rate (mpy) = - 2648 + 3.73 Thermal Treatment Temperature - 1077 Acid Concentration - 60.7 Grain Size 2 + 915 Grain Size

Predictor	Coef	SE Coef	T	P
Constant	-2648	1615	-1.64	0.145
Thermal Treatment	3.7339	0.5477	6.82	0.000
Acid Concentration	-1077.1	573.4	-1.88	0.102
Grain Size 2	-60.74	34.85	-1.74	0.125
Grain Size	915.1	457.7	2.00	0.086

S = 55.6210 R-Sq = 91.3% R-Sq(adj) = 86.4%

Analysis of Variance

Source	DF	SS	MS	F	P
Regression	4	227983	56996	18.42	0.001
Residual Error	7	21656	3094		
Total	11	249638			

There are no replicates.

Minitab cannot do the lack of fit test based on pure error.

Source	DF	Seq SS
Thermal Treatment	1	115219
Acid Concentration	1	10915
Grain Size 2	1	89482

Unusual Observations

Obs	Thermal Treatment	Corrosion rate (mpy)	Fit	SE Fit	Residual	St Resid
9	250	448.6	346.8	32.2	101.8	2.24R

R denotes an observation with a large standardized residual.

No evidence of lack of fit (P >= 0.1).

Fig. 5.6 Regression results from Minitab software

5.1.6 Microstructural characterization after corrosion measurements

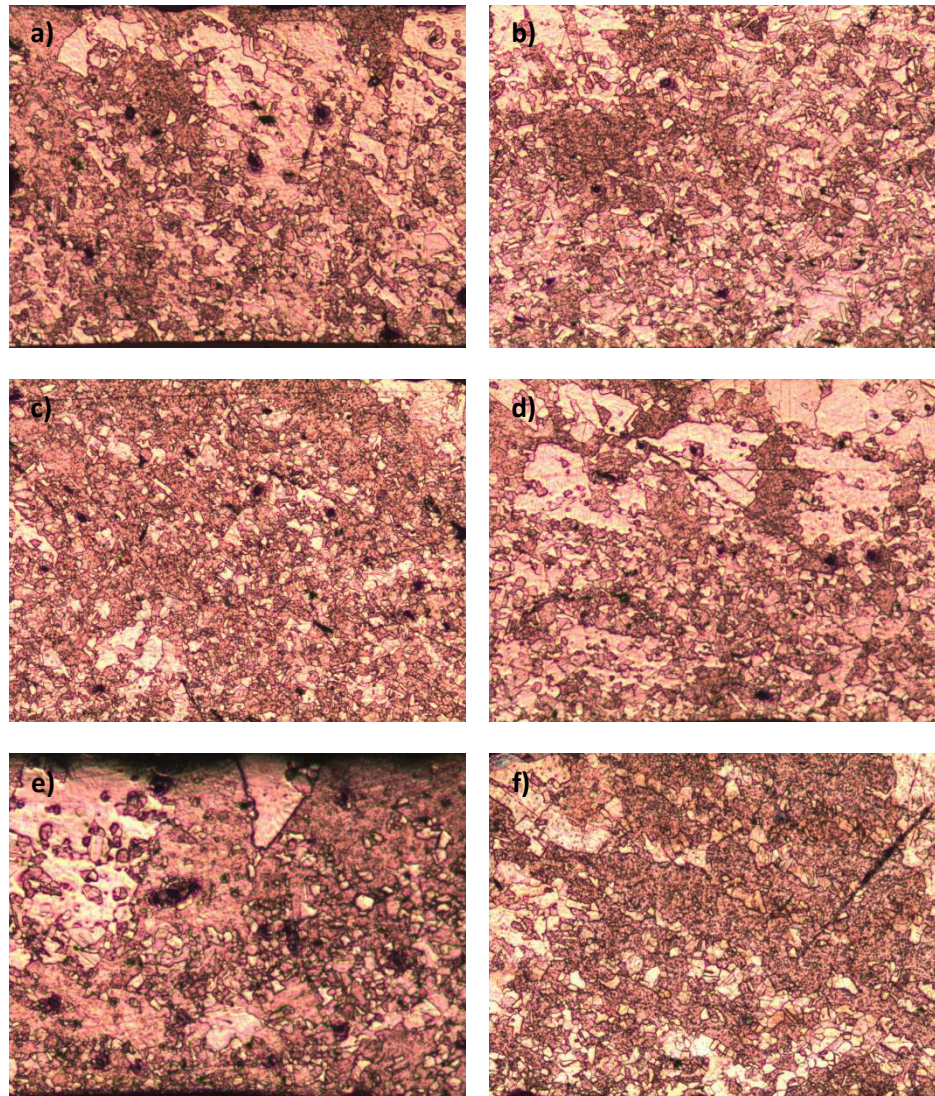


Fig. 5.7 Microstructure of Pb-Sn alloy at 100x after corrosion measurements; (a) TT 175 °C cooling 0°C; (b) TT 250 °C cooling 0°C; (c) TT 175 °C cooling 25°C; (d) TT 250 °C cooling 25°C; (e) TT 175 °C cooling 50°C; (f) TT 250 °C cooling 50°C

The effects of surface change of the samples after electrochemical attack is shown in Figure 5.7. In this figure, can be appreciated that samples experienced considerable damage, especially those samples that were treated at 175 °C of heating temperature.

5.1.7 General results

According to Figure 5.8, the relationship between grain size and corrosion rate varies according to acid concentration used for each test, but the main controlling variable is the temperature used for the thermal treatments, which opens the possibility to the categorization of the degradation phenomena in two groups, the one of samples exposed to 250 °C and another of samples exposed to 175 °C; according to this division, the samples exposed at 175 °C show almost no change in the grain size or the corrosion rate and a slight difference given by the acid concentration. Contrarily, the samples treated at 250 °C showed larger difference on the grain size and corrosion rates, also a larger difference given by the acid concentration. This suggests that the temperature of 175 °C is not enough to produce an important change on the behavior of either grain size or corrosion rate, as it is shown by the samples that were exposed to 250°C.

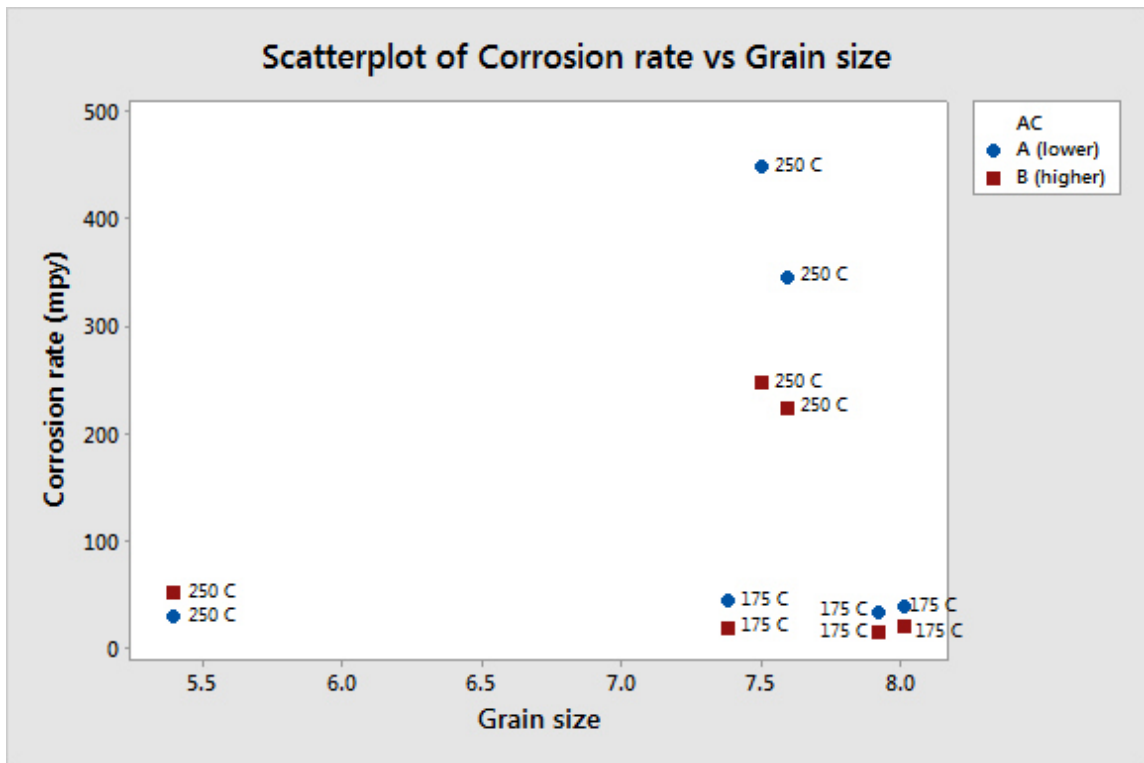


Fig. 5.8 Relationship between grain size and corrosion rate by thermal treatment temperature and by acid concentration

CHAPTER 6 CONCLUSIONS

6.1 Conclusions

- Different thermal treatments generated different microstructures allowing to study its effects on micro-hardness, mechanical properties and corrosion rates.
- A regression equation could be obtained to describe the effects of thermal treatment temperatures, cooling temperatures and acid concentration in the corrosion rate of Pb-Sn alloys with a relative high accuracy for an experimental work.
- No significant difference among heat treatments was found in micro-hardness results, probably given because the time or the temperature of thermal treatments was not enough to promote the diffusion of Sn, at least not at a range that has an impact on the micro-hardness of the alloy.
- Regarding mechanical properties, samples treated at 175 °C showed higher strain at break than those samples treated at 250 °C. Samples treated at 250 °C showed values of strain at break (%) and peak stress (MPa) even smaller than the master sample.
- Corrosion rates (mpy) for samples that were treated at 250 °C, are considerably higher than the corrosion rates that those samples that were treated at 175 °C. This is probably given by the difference in the grain size, it can be said that coarse cellular structures tend to yield higher corrosion resistance than fine cellular morphology.
- The effect of cooling temperature is not linear, smaller corrosion rates are shown in samples that were cooled at 0 °C, which agrees with previous works that reinforces the effect of the cooling rate in the electrochemical behavior of lead alloys.
- Corrosion rates at acid concentration B are smaller than with acid concentration A, as expected, the lower the acid concentration is, the

fastest the passive layer is dissolved, therefore, the highest the corrosion rate.

- The smaller corrosion rate was generated with the combination of the following factors: thermal treatment temperature 175 °C, cooling temperature 50 °C and acid concentration B.

6.2 Recommendations

- For Pb-Sn alloys the effect of higher temperatures should be studied in order to obtain different microstructures and evaluate its effect on the corrosion rate.
- Given that Pb-Sn alloys are widely used for lead-acid batteries in order to improve batteries performance the effect of selenium at different concentrations should be studied further to evaluate its effect on the corrosion rate.

REFERENCES

1. *Microstructure and electrochemical corrosion behavior of a Pb-1 wt% Sn alloy for lead-acid battery components.* **Peixoto, L., Osório, W., Garcia, A.** 724-729, s.l. : Journal of Power Sources, 2009, Vol. 192.
2. *The interrelation between mechanical properties, corrosion resistance and microstructure of Pb-Sn casting alloys for lead-acid battery components.* **Peixoto, L., Osório, W., Garcia, A.** 621-630, s.l. : Journal of Power Sources, 2010, Vol. 195.
3. **Kiehne, H.A.** *Battery Technology Handbook.* s.l. : CRC Press, 2003.
4. **Linden, D.** *Handbook of Batteries.* s.l. : McGraw-Hill, 2002.
5. **Dell, R.M., Rand, D.A.J.** *Understanding Batteries.* s.l. : Royal Society of Chemistry, 2001.
6. **D.A.J. Rand, P.T. Moseley, J. Garche, C.D. Parker.** *Valve-regulated Lead-Acid Batteries.* s.l. : ELSEVIER, 2004.
7. **Rand, D.A.J.** *Valve-regulated Lead-Acid Batteries.* s.l. : ELSEVIER, 2004.
8. *Characterisation of defects observed within the positive grid corrosion layer of the valve regulated lead-acid batteries.* **Ball, R. J., Evans, R., Deven, M., Stevens, R.** 201-212, s.l. : Journal of Power Sources, 2002, Vol. 103.
9. **Davis, J.R.** *Corrosion: Understanding the basics.* s.l. : ASM International, 2000.
10. **Halici, S.** *Development of lead alloys for valve regulated lead-acid batteries.* s.l. : Middle East Technical University, 2010.
11. **McCafferty, E.** *Introduction to Corrosion Science.* s.l. : Springer, 2010.
12. **Perez, N.** *Electrochemistry and Corrosion Science.* s.l. : Kluwer Academic Publishers, 2004.
13. **Pavlov, Detchko.** *Lead-Acid Batteries: Science and Technology.* s.l. : ELSEVIER, 2011.

14. *Manufacturing and operational issues with lead-acid batteries.* **Rand, D.A.J., Boden, D.P, Lakshmi, C.S.** 280-300, s.l. : Journal of Power Sources, 2002, Vol. 107.
15. **Schweitzer, Philip A.** *Fundamentals of corrosion.* s.l. : CRC Press, 2010.
16. **Gurusguamy, S.** *Engineering Properties and Applications of Lead Alloys.* s.l. : Marcel Dekker, Inc., 2000.
17. **Winston, R.** *Uhlig's Corrosion Handbook.* s.l. : The Electrochemical Society, 2011.
18. *Influence of positive active material type and grid alloy on corrosion layer structure and composition in the valve regulated lead-acid battery.* **Ball, R. J., Kurian, R., Evans, R., Stevens, R.** 23-38, s.l. : Journal of Power Sources, 2002, Vol. 111.
19. **International, ASTM.** *ASTM-E345 Standard Test Methods of Tension Testing of Metallic Foil.* 2013.
20. *Influence of the cooling rate on the ageing of lead–calcium alloys.* **F. Rossi, M. Lambertin, L. Delfaut-Durut, A. Maitre, M. Vilasi.** 296-300, s.l. : Journal of Power Sources, 2009, Vol. 188.
21. *Electrochemical corrosion of Pb–1 wt% Sn and Pb–2.5 wt% Sn alloys for lead-acid battery applications.* **Osório, W., Peixoto, L., Garcia, A.** 1120-1127, s.l. : Journal of Power Sources, 2009, Vol. 194.
22. *Effect of solidification temperature of lead alloy grids on the electrochemical behavior of lead-acid battery.* **B. Rezaei, S. Damiri.** 590-594, s.l. : Solid State Electrochem, 2005, Vol. 9.

LIST OF FIGURES

- 1.1 Discharge and charge reactions of lead-acid cell: (a) Discharge reactions; (b) Charge reactions (2)
- 1.2 Conceptual view of internal oxygen cycle in a valve-regulated lead-acid cell (4)
- 2.1 Schematic representation of anodic and cathodic polarization (10)
- 2.2 Schematic representation of anodic and cathodic polarization (9)
- 2.3 Corrosion at negative plate lugs that occasionally is observed. Current flow along the wetting layer of the non-immersed parts causes a potential shift within that layer. Thus, 'cathodic corrosion protection' may no longer exist above a certain distance from the electrolyte level. The situation is influenced by the alloys used in the parts and for welding (1)
- 3.1 Pb-Sn Phase diagram (14)
- 3.2 Micrographs showing effects of calcium and tin additions on microstructure of: (a) Pb-0.06 wt. % Ca-0.6 wt. % Sn; (b) Pb-0.13 wt. % Ca-0.6 wt. % Sn; (c) Pb-0.06 wt. % Ca-1.5 wt. % Sn (12)
- 3.3 Typical microstructures observed along at longitudinal sections and at different locations (5, 10, 15, 20, 30, 40, 50, 60 and 70mm) from the bottom of the casting for the Pb-1 wt% Sn alloy (optical magnification: 125x) (15)
- 3.4 Typical microstructures observed along at longitudinal sections and at different locations (5, 10, 15, 20, 30, 40, 50, 60 and 70mm) from the bottom of the casting for the Pb-2.5 wt% Sn alloy (optical magnification: 125x) (15)
- 3.5 Typical stress-strain curves as a function of cellular spacing: (a) Pb-1 wt% Sn and (b) Pb-2.5 wt% Sn alloys (15)

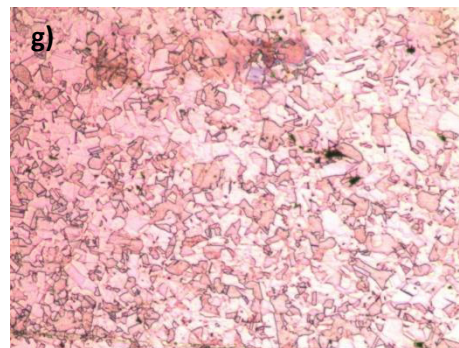
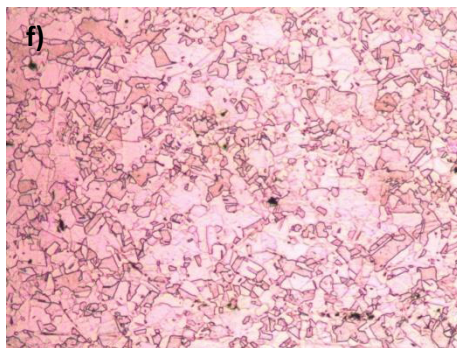
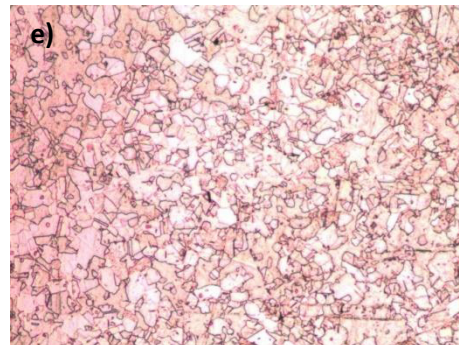
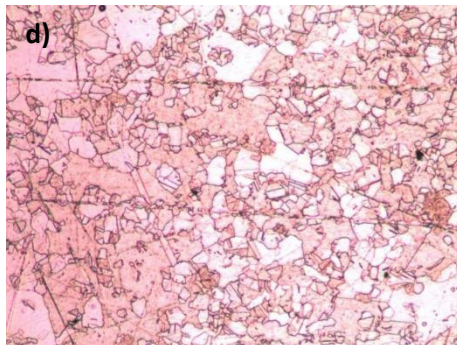
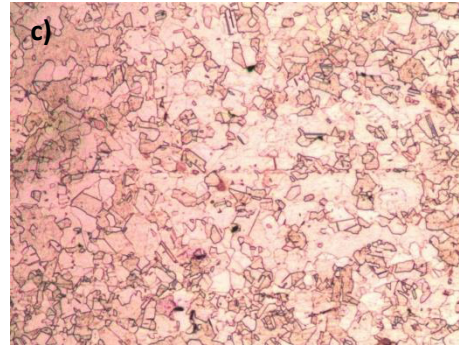
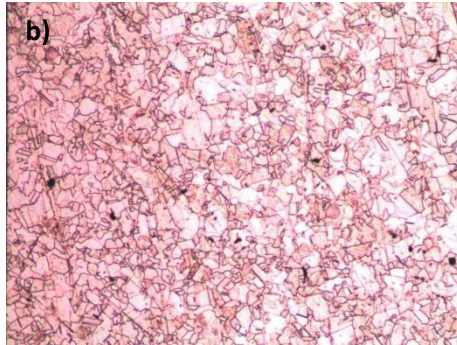
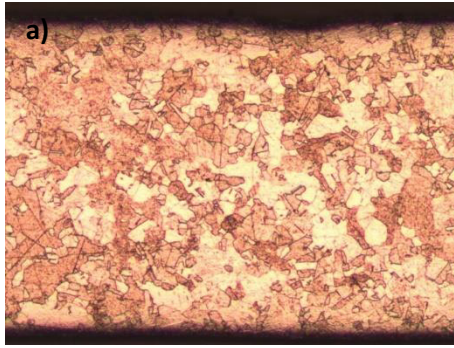
- 3.6 Corrosion rate of lead in sulfuric acid (16)
- 3.7 Weight losses of Pb-2.0 wt% Sn electrodes with time of stay at 50 °C in oxygen atmosphere (11)
- 3.8 Corrosion transients for Pb-2.0 wt% Sn and Pb-2.0 wt% Sn-0.03 wt% Se electrodes partly inserted in AGM soaked in (a) H₂SO₄ and (b) H₂SO₄ + Na₂SO₄ solution (11)
- 4.1 Experimental flow chart
- 4.2 Cutting samples to strips
- 4.3 (a) Sample machining to “dog bone” shape; (b) “dog bone” shaped samples
- 4.4 Mettler-Toledo arch and spark spectrometer
- 4.5 Diagram of thermal treatments for Pb-Sn binary alloys
- 4.6 Thermal treatments for Pb-Sn binary alloys at 175 °C with 3 different cooling temperatures
- 4.7 Thermal treatments for Pb-Sn binary alloys at 250 °C with 3 different cooling temperatures
- 4.8 Mechanical Convection Oven 625 FREAS used for thermal treatments
- 4.9 Variable Speed Grinder-Polisher EcoMet 3000 BUEHLER used for sample polishing
- 4.10 MCA UNITRON MODZST microscope
- 4.11 Micro-durometer Wilson Instron Tukon 2100 for micro-hardness measuring
- 4.12 Universal testing machine MTS Sintech 1/G
- 4.13 a) Samples mounted as work electrodes, b) Exposed surface for corrosion rate measuring
- 4.14 Surface area measuring with software Image-Pro Plus
- 4.15 (a) Work, counter electrode and reference electrodes; (b) Samples arrangement with Potentiostat/Galvanostat
- 4.16 Princeton Applied Research / EG&G Model 273 Potentiostat/Galvanostat

- 5.1 Microstructure of Pb-Sn alloy at 100x (a) initial; (b) TT 175 °C cooling 0°C; (c) TT 250 °C cooling 0°C; (d) TT 175 °C cooling 25°C; (e) TT 250 °C cooling 25°C; (f) TT 175 °C cooling 50°C; (g) TT 250 °C cooling 50°C
- 5.2 Measurements for micro-hardness
- 5.3 Mechanical properties of samples heat treated at 175 °C
- 5.4 Mechanical properties of samples heat treated at 250 °C
- 5.5 Main effects plot for corrosion rate
- 5.6 Regression results from Minitab software
- 5.7 Microstructure of Pb-Sn alloy at 100x after corrosion measurements; (a) TT 175 °C cooling 0°C; (b) TT 250 °C cooling 0°C; (c) TT 175 °C cooling 25°C; (d) TT 250 °C cooling 25°C; (e) TT 175 °C cooling 50°C; (f) TT 250 °C cooling 50°C
- 5.8 Relationship between grain size and corrosion rate by thermal treatment temperature and by acid concentration

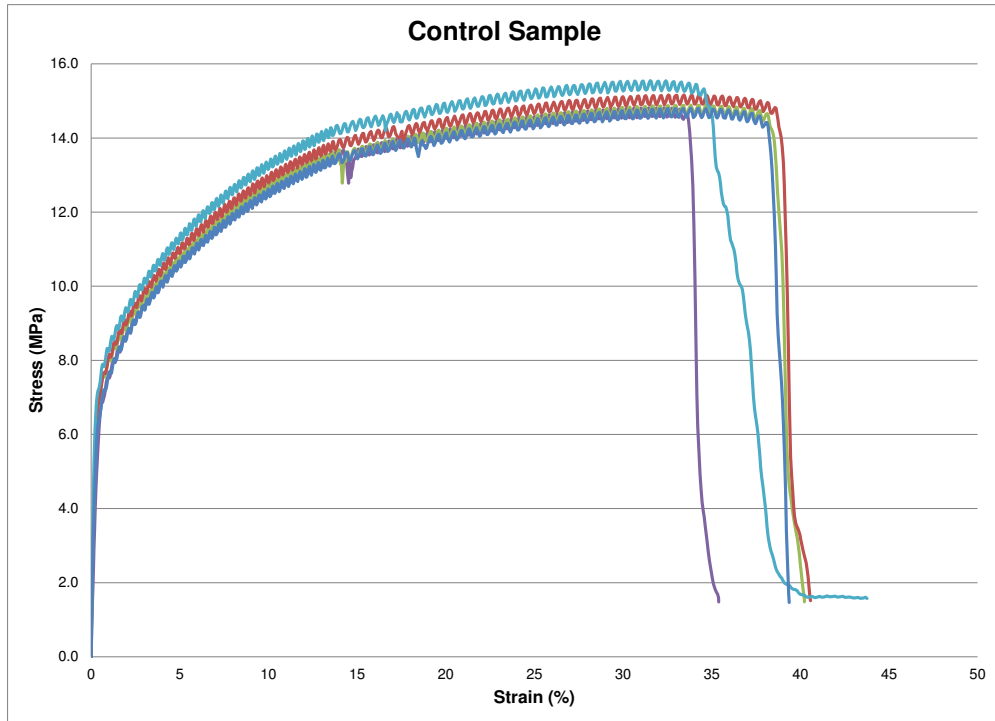
LIST OF TABLES

- 3.1 Required mechanical properties of lead-acid battery grids (11)
- 3.2 Mechanical properties of Pb-1.0 wt% Sn alloys with or without 0.06 wt% Ca (11)
- 5.1 Grain size results for each thermal treatment
- 5.2 Micro-hardness results for each thermal treatment
- 5.3 Mechanical properties of the samples for each thermal treatment
- 5.4 Corrosion rate results for each thermal treatment and acid concentration

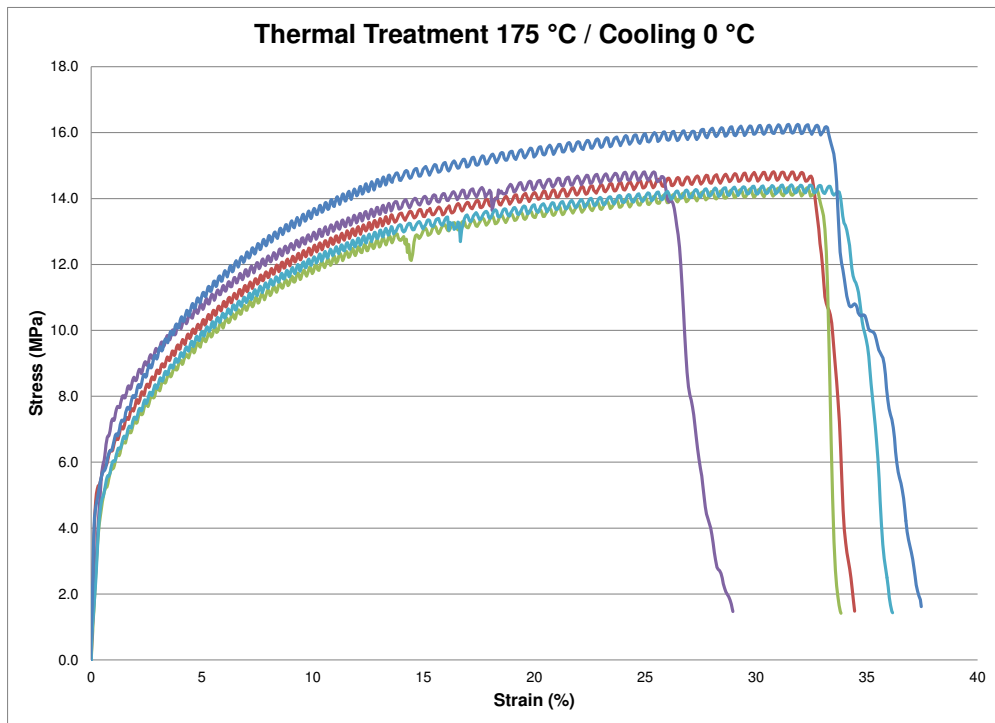
APPENDIX



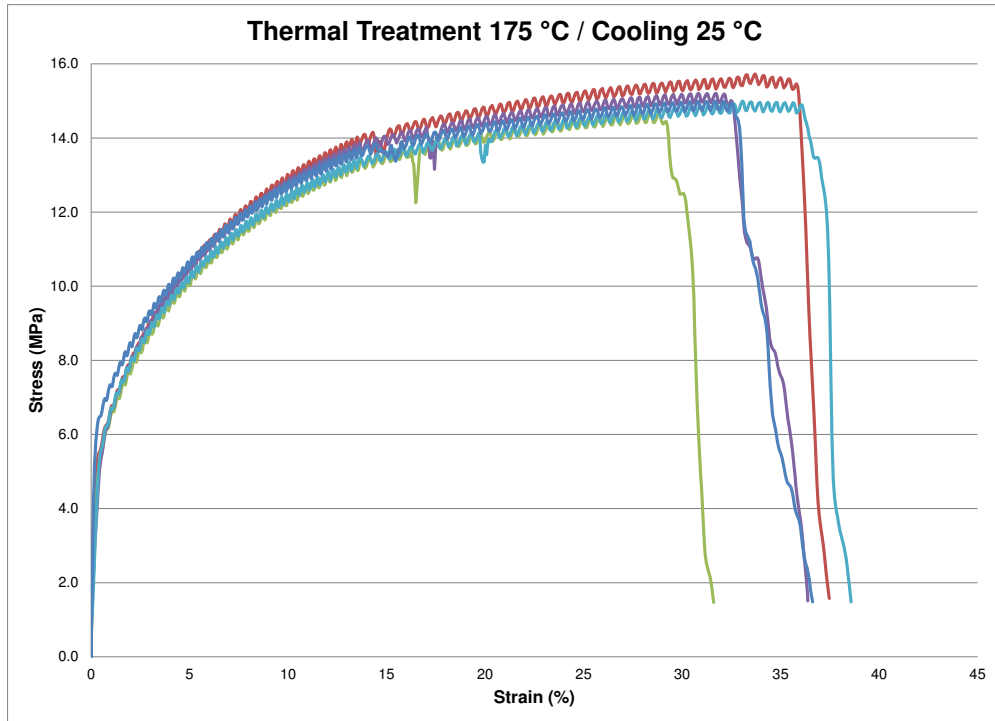
Microstructure of Pb-Sn alloy at 50x a) initial, b) TT 175 °C cooling 0°C, c) TT 250 °C cooling 0°C, d) TT 175 °C cooling 25°C, e) TT 250 °C cooling 25°C, f) TT 175 °C cooling 50°C, g) TT 250 °C cooling 50°C



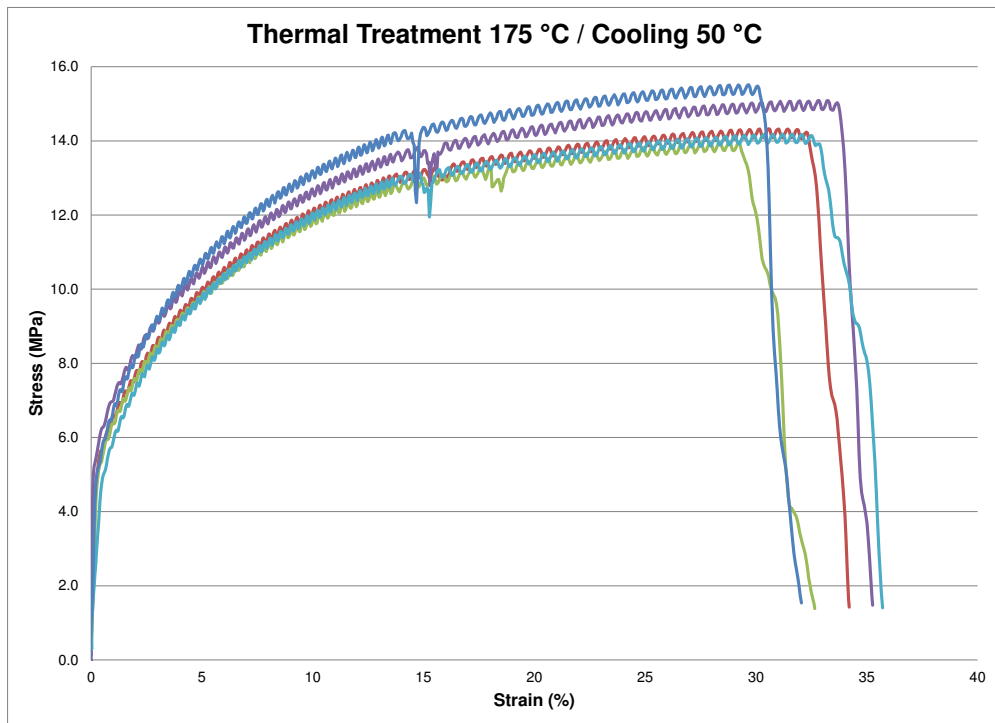
Mechanical properties: control sample



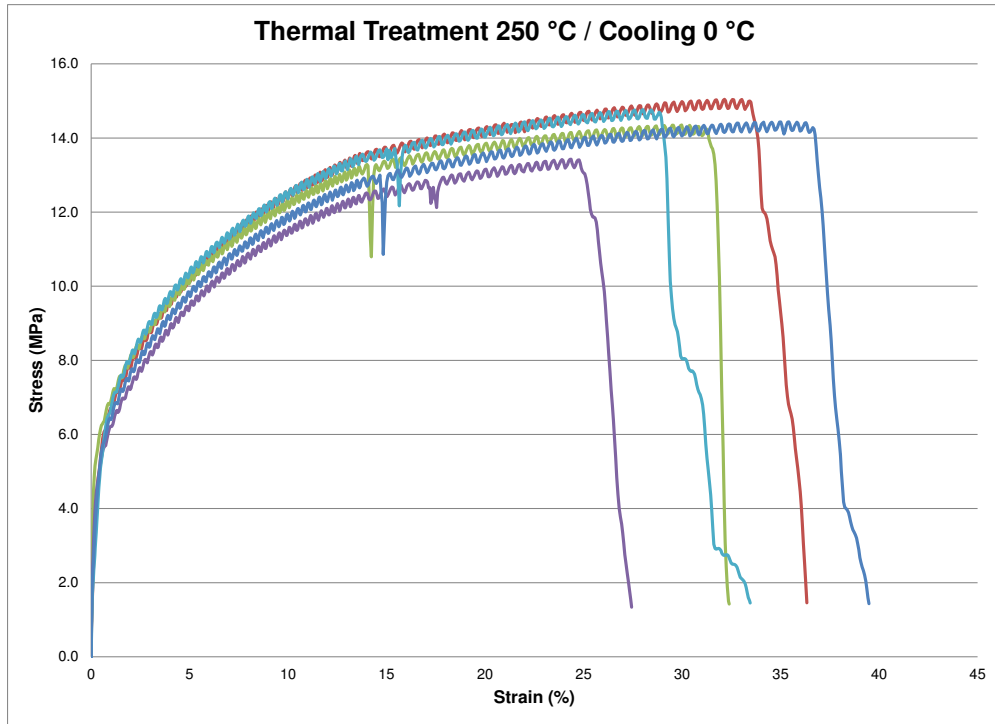
Mechanical properties: thermal treatment temperature 175 °C, cooling temperature 0 °C



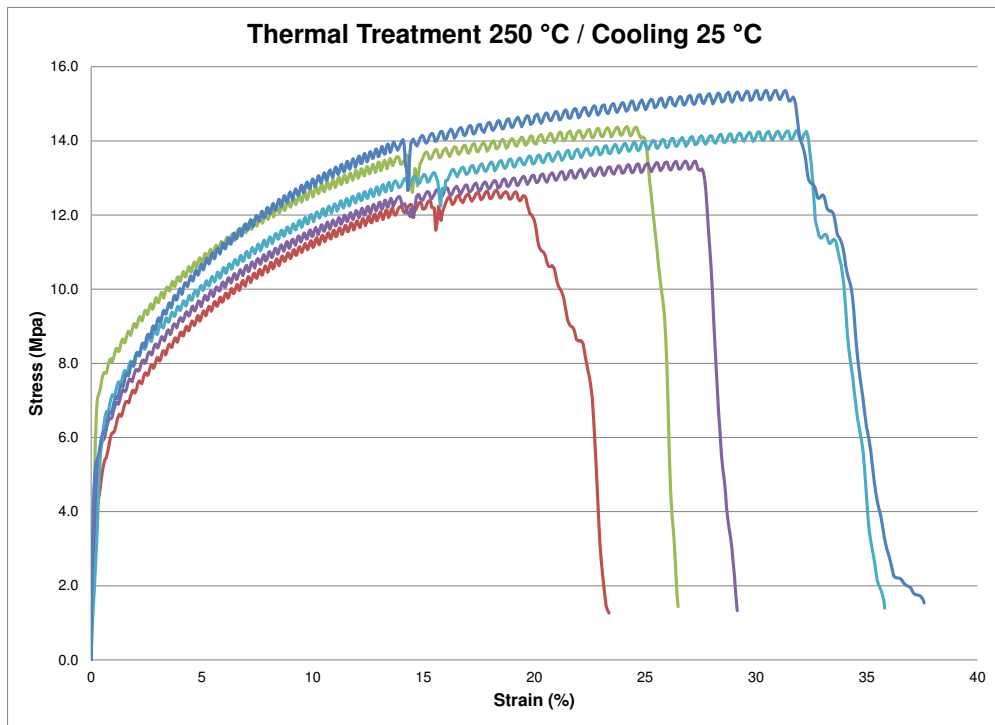
Mechanical properties: thermal treatment temperature 175 °C, cooling temperature 25 °C



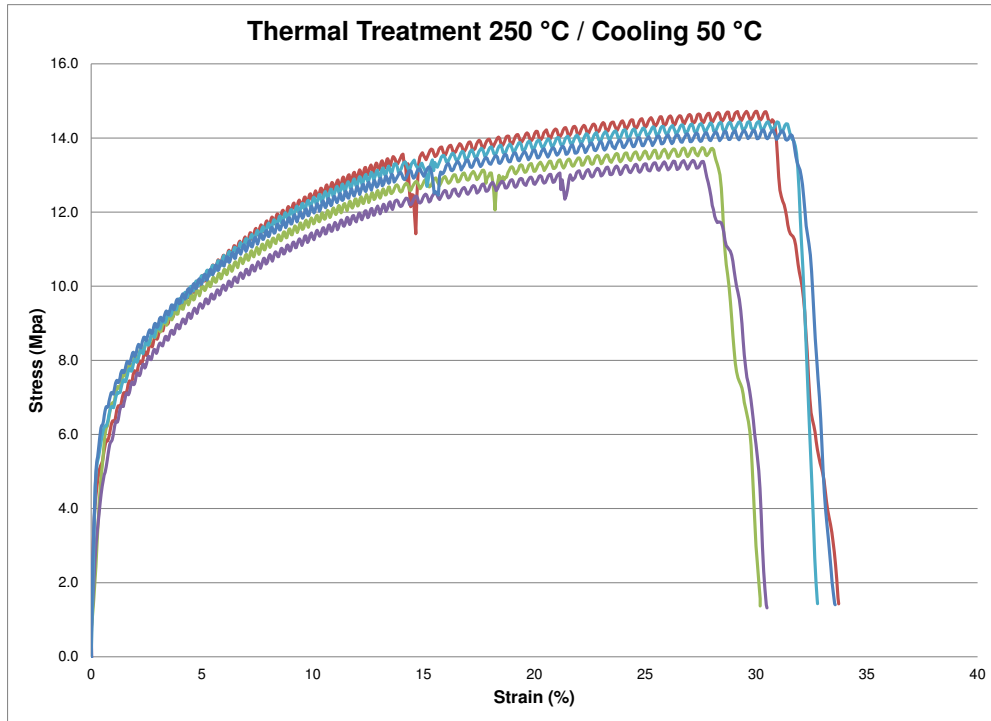
Mechanical properties: thermal treatment temperature 175 °C, cooling temperature 50 °C



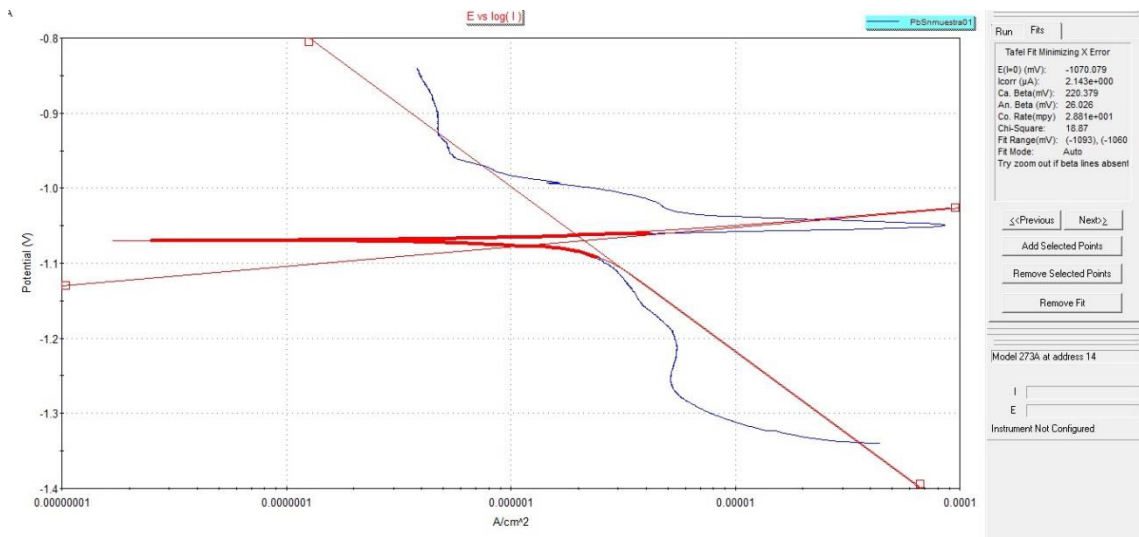
Mechanical properties: thermal treatment temperature 250 °C, cooling temperature 0 °C



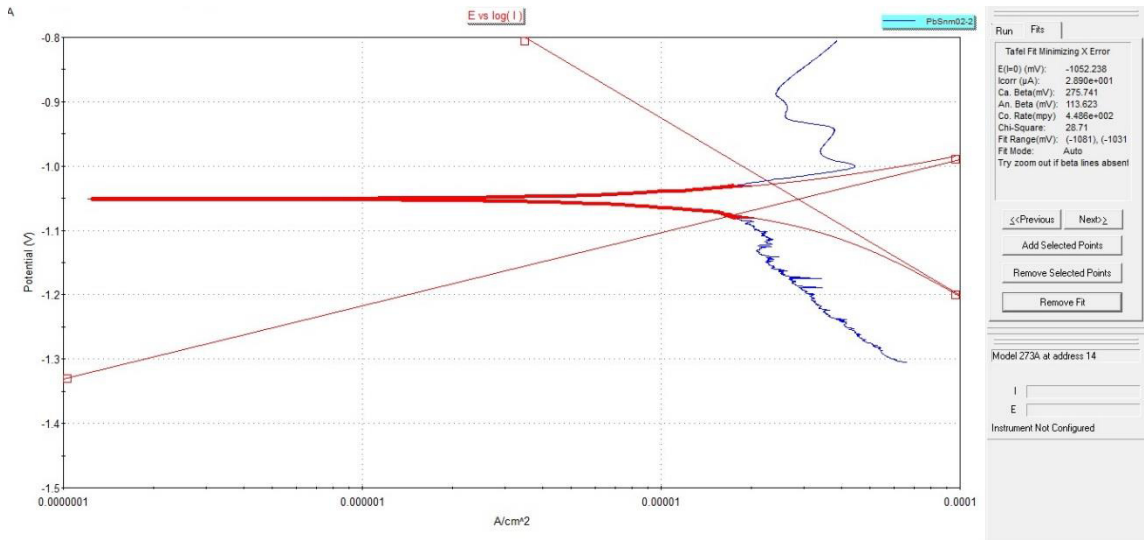
Mechanical properties: thermal treatment temperature 250 °C, cooling temperature 25 °C



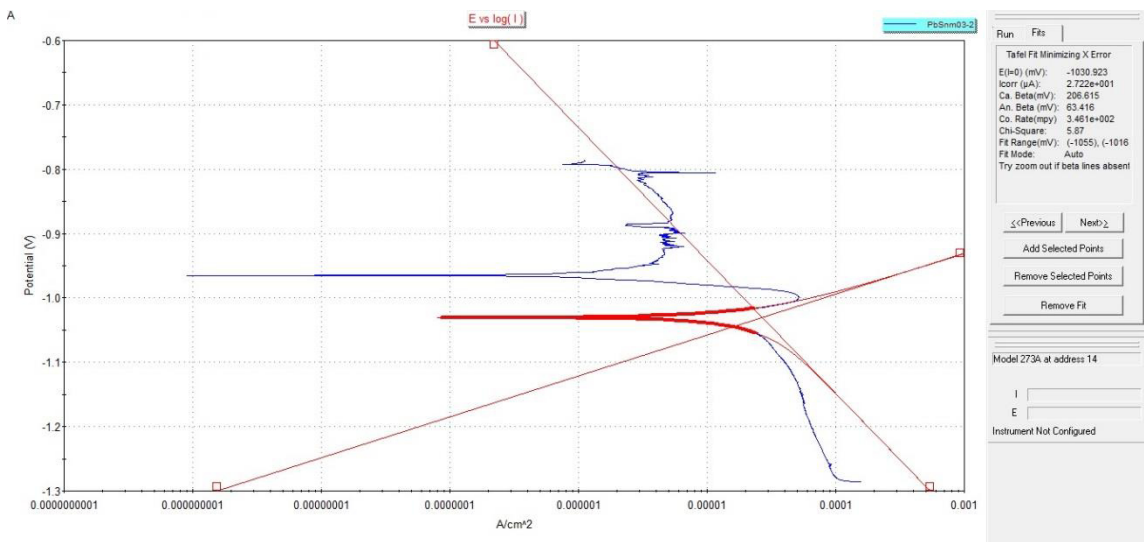
Mechanical properties: thermal treatment temperature 250 °C, cooling temperature 50 °C



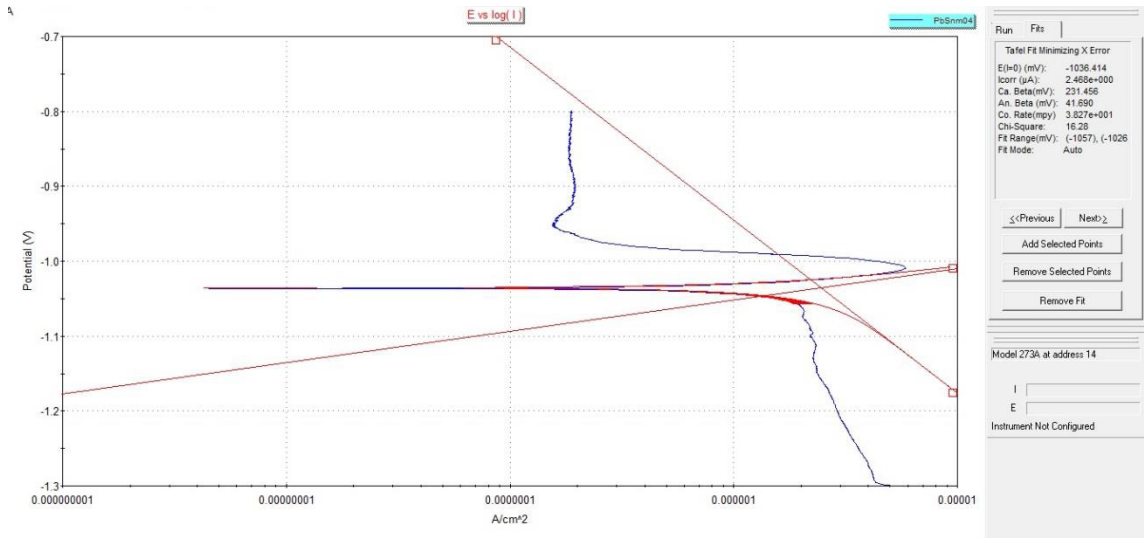
Tafel slope: Sample 1 Acid Concentration A



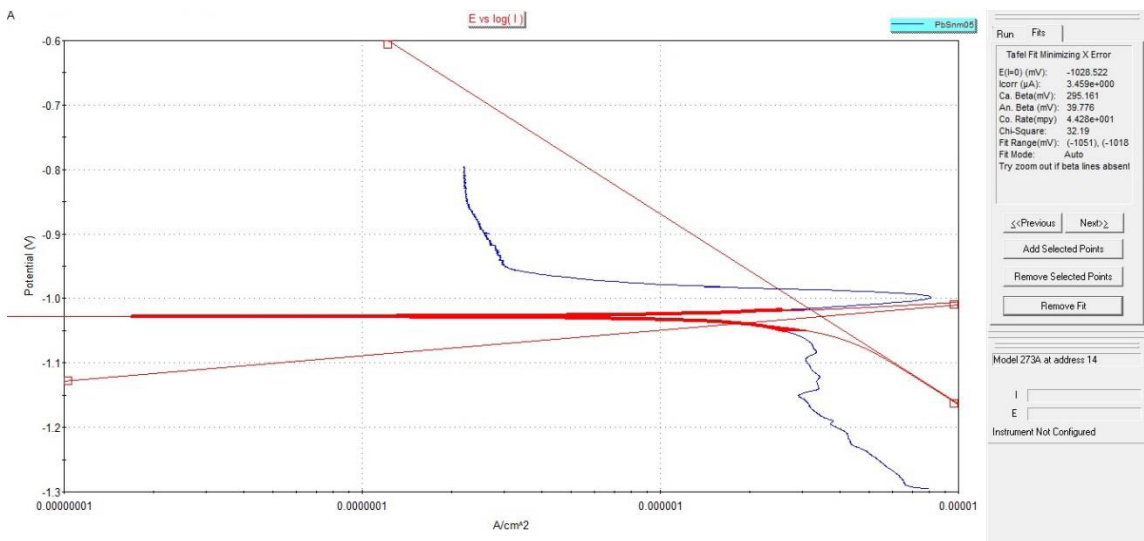
Tafel slope: Sample 2 Acid Concentration A



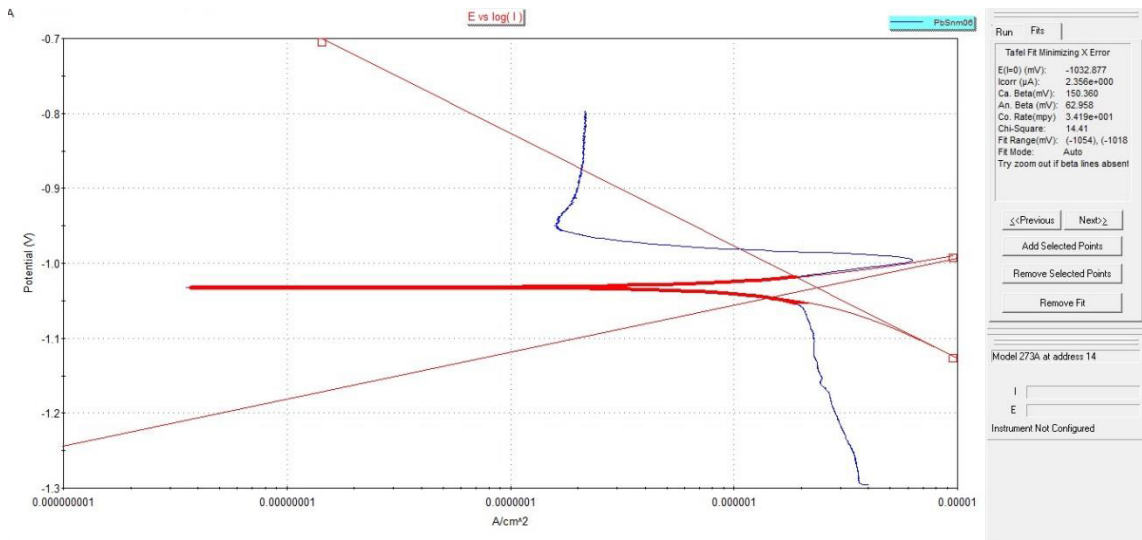
Tafel slope: Sample 3 Acid Concentration A



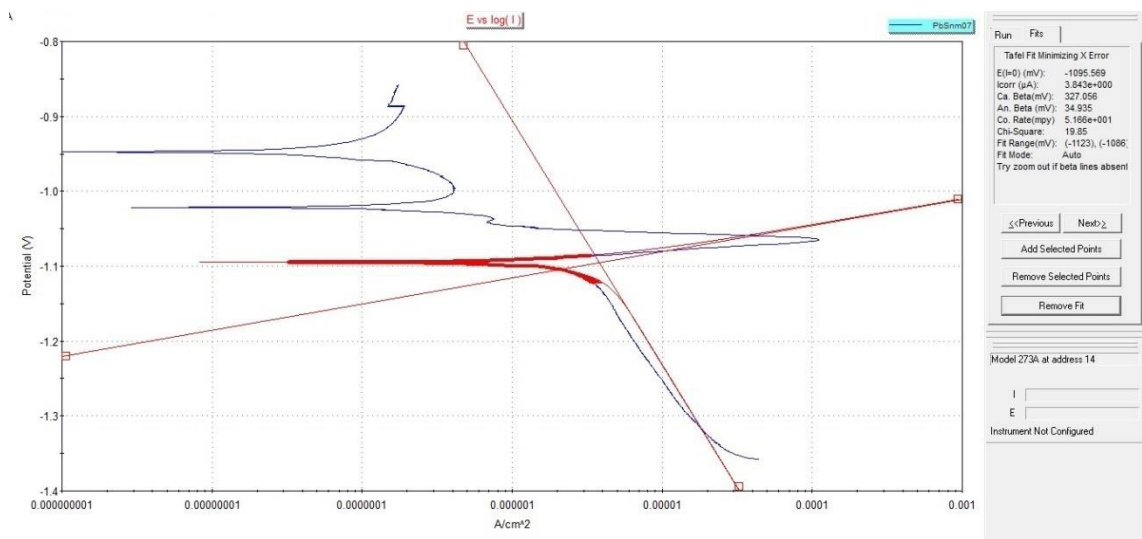
Tafel slope: Sample 4 Acid Concentration A



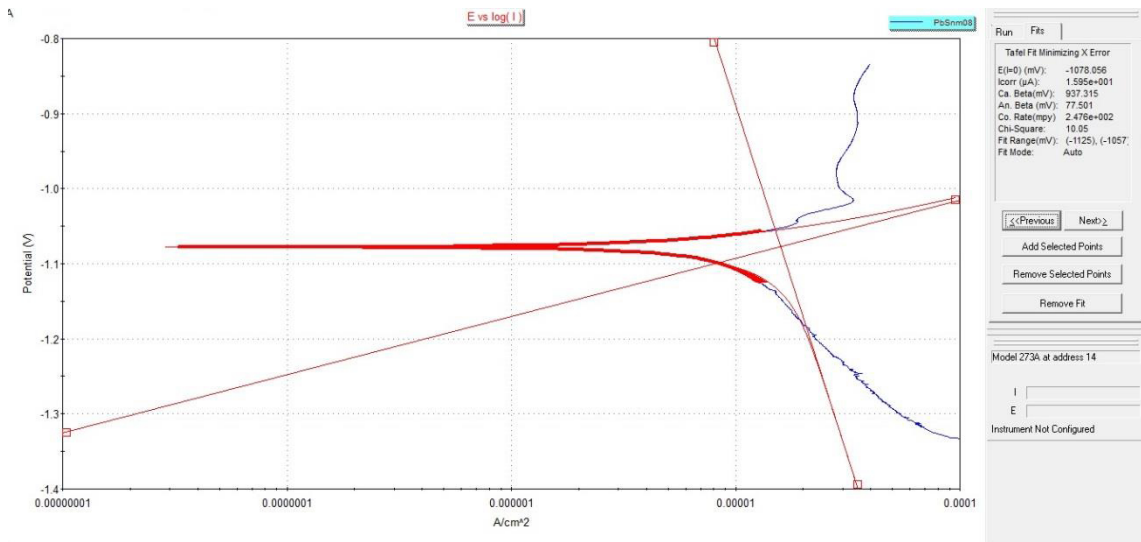
Tafel slope: Sample 5 Acid Concentration A



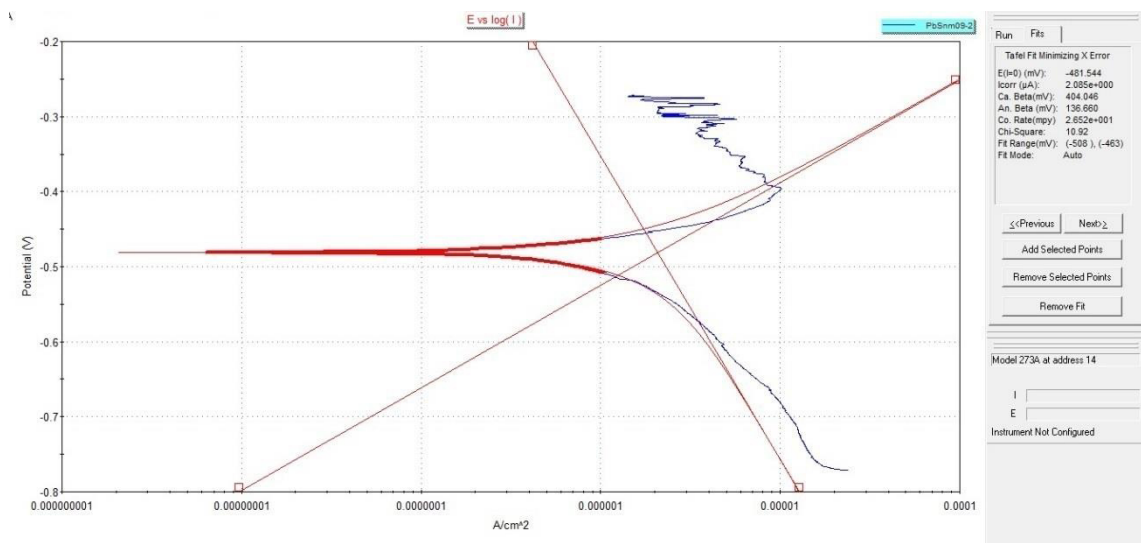
Tafel slope: Sample 6 Acid Concentration A



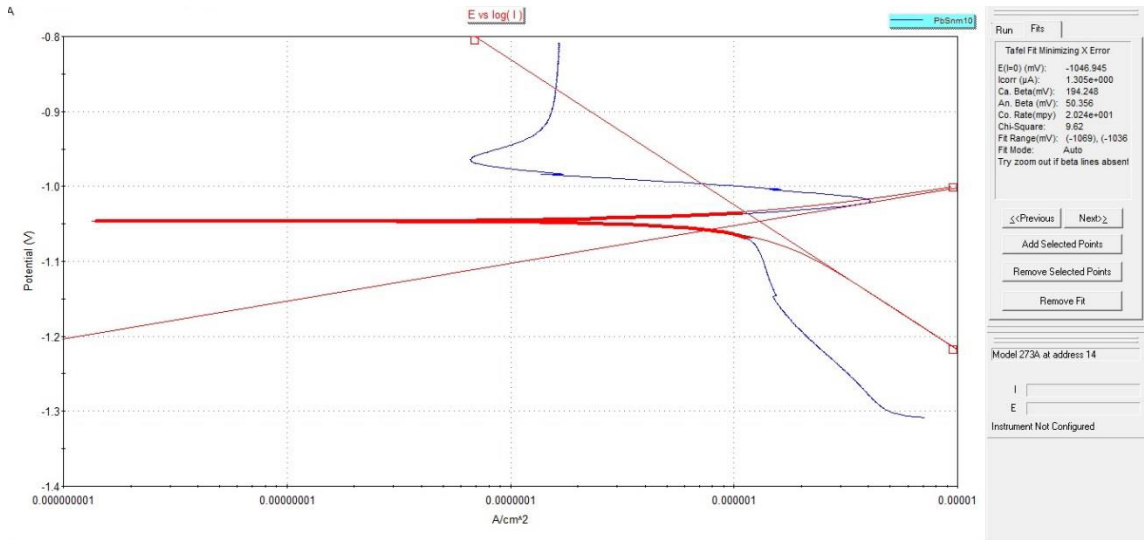
Tafel slope: Sample 1 Acid Concentration B



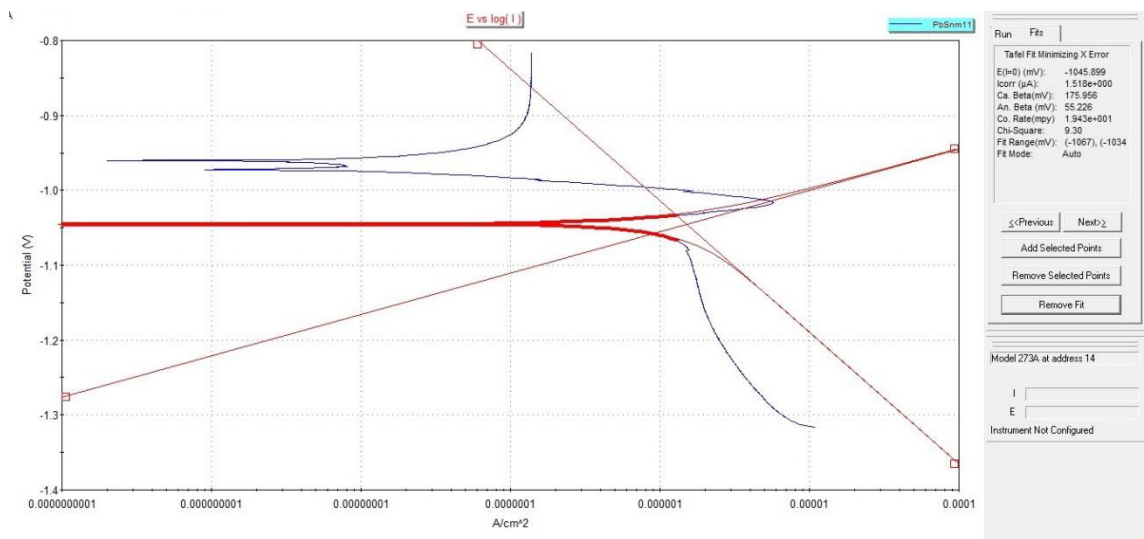
Tafel slope: Sample 2 Acid Concentration B



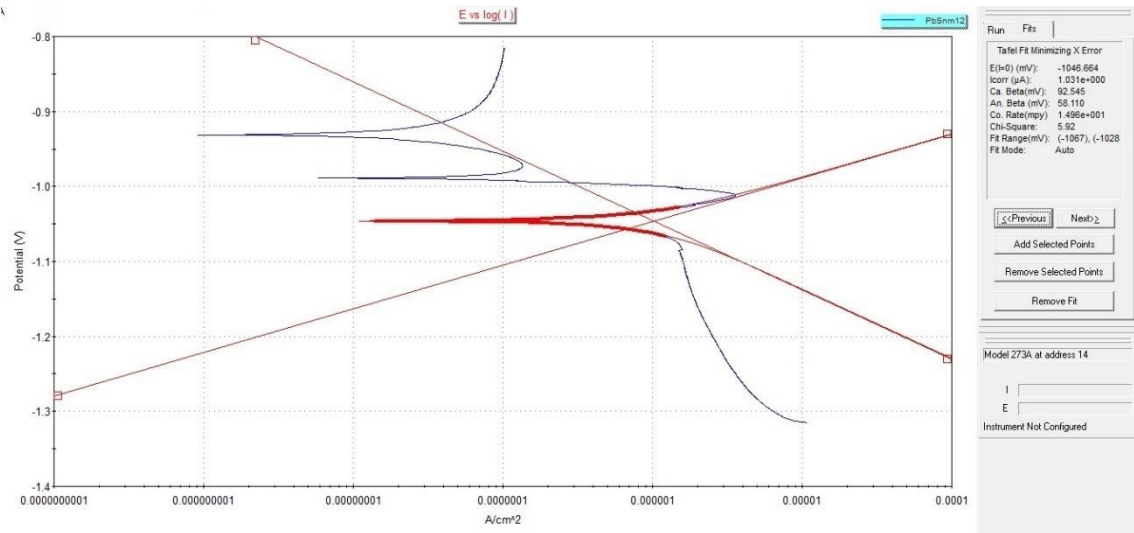
Tafel slope: Sample 3 Acid Concentration B



Tafel slope: Sample 4 Acid Concentration B



Tafel slope: Sample 5 Acid Concentration B



Tafel slope: Sample 6 Acid Concentration B